Unified Framework for Osmotic Energy Conversion

Oren Lavi,[†] Ramadan Abu-Rjal,[†] and Yoav Green[*]
Department of Mechanical Engineering, Ben-Gurion University of the Negev, Beer-Sheva, Israel

(Received 28 December 2025; revised 28 July 2026; accepted 13 August 2026; published 16 September 2026)

Osmotic energy systems employ charged nanoporous membranes and nanochannels to convert salinity gradients into electrical power, offering a promising route to harvest one of Earth's most abundant yet underexploited renewable resources—the oceans—and providing reliable, carbon-free electricity. However, to date, no known self-consistent theoretical model can accurately predict the electrical response of realistic charge-selective systems. Thus, empirical and phenomenological models are used to increase the performance while attributing the increase to various mechanisms, which are mostly incorrect and incomplete. This leads to a costly empirical trial-and-error optimization process, which typically yields only incremental improvements. Here, we provide a self-consistent theoretical model for the current-voltage ($I-V$) response, verified by nonapproximated numerical simulations, that establishes a detailed framework for osmotic energy conversion in realistic systems comprising a charge-selective membrane and the often-neglected larger bulk reservoirs. Our model delineates the effects of the surface charges, the bulk concentration ratio, and the often-neglected effects of the bulk reservoirs. The model provides analytical expressions for all the major transport characteristics at zero current ($I=0$), including the Ohmic resistance, R_{Ohmic}, the voltage at zero current, $V_{I=0}$, and the transport number, τ, which is a metric for the selectivity of the system. The $I=0$ insights are carried over to the results at the energy harvesting limit of zero voltage ($V=0$), allowing a straightforward analysis. Two of our key results are unexpected. First, the concentration at which the harvestable electrical power is maximal is not the concentration at which the harvestable electrical current is maximal. Second, overlooking the effects of the bulk reservoirs leads to overestimations of the harvestable power by several orders of magnitude. Our proposed framework lays the theoretical foundation for a new generation of sustainable nanofluidic energy systems relevant to addressing global energy and water challenges.

DOI: 10.1103/xnd6-226l

I. INTRODUCTION

Ion transport across charge-selective nanosized channels is ubiquitous in both nature and technology. In physiological systems, these channels are biological ion channels that regulate basic physiological phenomena [1–3]. In technological applications like water desalination and energy harvesting systems that utilize electrodialysis (ED) [4–7] and reverse-electrodialysis (RED) [8–13] processes, large-scale nanoporous membranes are used—these are multipore systems [14]. At the same time, biosensing [15–22] and DNA sequencing [22–27] systems utilize nanopores.

Interestingly, the emphasis and interests of RED and physiology are rather complementary. In RED, the desired quantity of interest is the energy that can be harvested through the zero-voltage current. In physiology, the desired quantity of interest is the electric potential barrier that needs to be overcome for physiological events to occur, characterized by the zero-current voltage. However, since all transport characteristics are derived from the same governing equations, knowledge of one limit implicitly leads to knowledge of the other. More importantly, this also implies that knowledge from the various fields of research can be transferred and exchanged between them.

While there is a nontrivial change in the geometry of these systems, as well as in the surface charge distribution (which can be either constant or spatially varying) and in other environmental conditions (such as salt concentration gradients and more), to the point that it can be claimed that all these systems are different, in reality, all these systems behave in a universal manner. The universality of the response can be attributed to the fact that in all scenarios, the physics (i.e., the governing equations and boundary

[*]Contact author: yoavgreen@bgu.ac.il
[†]These authors contributed equally to this work.

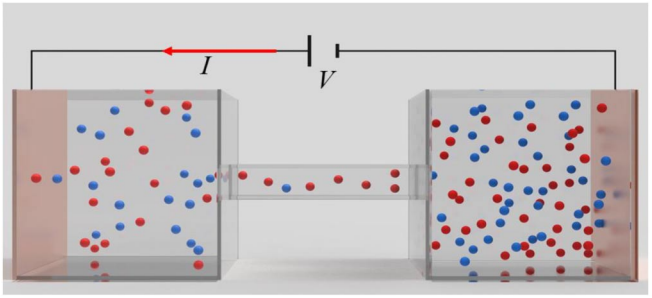

FIG. 1. Schematic of a realistic nanofluidic system comprised of an ion-selective nanochannel flanked by two microchannels containing a binary electrolyte with different salt concentrations (c_{left} and c_{right}). The entire system is subject to a voltage drop, V (defined as positive from left to right), resulting in an electrical current, I. A surface charge density (not shown here but shown in Fig. 2) results in an excess of counterions, represented by red spheres, over the coions, represented by blue spheres.

conditions) is the same. To understand this universality, it is essential to isolate the shared features of these systems. Figure 1 schematically depicts a universal system with its three key components:

(1) Two electrodes are connected to a voltage source that applies a voltage, V, resulting in an electrical current, I (or vice versa, a current source and a resultant voltage). Regardless, all these systems are characterized by their steady-state current-voltage, $I-V$, response.

(2) Two large reservoirs that have different bulk concentrations, which can be denoted as c_{left} and c_{right}. Although the solution is given in terms of c_{left} and c_{right}, it is useful to use the notation

$$C_r = c_{\text{right}}/c_{\text{left}}, \tag{1}$$

to describe systems with symmetric $(C_r = 1)$ and asymmetric $(C_r \neq 1)$ bulk concentrations.

(3) The large reservoirs are connected by a much smaller charged channel, which is responsible for the symmetry-breaking result of ion selectivity. This smaller channel can be an ion channel, a nanochannel, a nanopore, or a nanoporous membrane. For clarity, throughout this work, we will denote this as the "nanochannel." In the subsection below, we shall clarify how the geometries of all these various systems are related to the "nanochannel."

In all of the above-mentioned systems and applications, the variation is not in the existence of these components but in how the $I-V$ varies as the geometry, the surface-charge distribution, and C_r are varied. Importantly, to date, the system depicted in Fig. 1, comprising a nanochannel connecting two microchannels and subjected to an arbitrary concentration gradient, has not yet been fully considered in detail and in a self-consistent manner.

It is interesting to note that concentration-induced ion transport across a charge-selective membrane has a long history, dating back to the experimental work of Ref. [28]. However, theoretical works on these systems [29,30] oversimplified their analysis by neglecting the effects of the reservoirs (all these models correspond to what will soon be termed a 1L system) and assuming ideal selectivity, such that, in practice, their solution held only for low concentrations and could not be extended to realistic nonideally selective systems (where one solution is very low and the other is exceedingly high). Later phenomenological works [31–34] extended this analysis from a single membrane to a stack of membranes by expressing the voltage as the sum of the various Nernst potentials across membrane pairs and using empirically measured (rather than analytically predicted) resistances. Here, too, ideal selectivity was imposed. It is also important to note that in all these works, the analysis was not internally consistent in that the electric potential and concentration distributions were decoupled. Moreover, the outcomes of the analysis were typically one characteristic (such as the power or the transmembrane potential), while all remaining characteristics were not calculated. In contrast, here we calculate the self-consistent interplay of the concentration and electric fields, without making any prior assumptions about selectivity, to yield *all* ion transport characteristics (such as the resistance, the transmembrane potential, the harvestable power, the transport number, and more).

The lack of a self-consistent theory has led to experiments relying either on a phenomenological model or on comparisons to idealized cases that neglect the all-important effects of the microchannels. This has led experimentalists to continuously tweak material properties, geometries, and other factors in a trial-and-error manner to improve the performance of RED systems. However, this approach is both time- and resource-costly and does not necessarily provide new and/or correct insights into how to improve the performance. Furthermore, due to the lack of physical clarity and the absence of a baseline model, experimentalists often define various figures of merit to compare different systems. The model presented in this work can be used to address these issues. First, it can be used as a baseline model. Second, since this model is deterministic, once the system parameters (geometry, concentration gradients, etc.) are set, there is no need for figures of merit (at least when considering KCl). Rather, since this model provides the "ideal" deterministic response of such systems, all experimental results can be compared to this ideal prediction, allowing for an even more direct comparison across all systems (including different materials).

This work is structured as follows. In Sec. II, we provide a short overview of the various systems/scenarios that have been investigated in past works. Each of the scenarios presented is a limiting scenario of the general scenario

derived in this work. In Sec. III, we present the physical and mathematical model, including the governing equations and boundary conditions (BCs), of our three-layered model subjected to an arbitrary concentration gradient. To avoid a lengthy derivation, which is similar to the derivation in several past works, we have moved the detailed derivation to Supplemental Material [35], while the main text focuses on the analysis of the two derived master equations.

Our analysis is divided into two dedicated results sections: Secs. IV and V. In Sec. IV, we focus on the main transport characteristics at the zero-current, $I = 0$, state. In particular, we discuss the behavior of the salt current density ($J_{I=0}$), transport number (τ), zero-current voltage ($V_{I=0}$), and resistance ($R_{I=0}$). In Sec. V, we shift focus to the transport characteristics at the zero-voltage, $V = 0$, state, discussing the behavior of the zero-voltage current ($I_{V=0}$), the resistance ($R_{V=0}$), and the harvestable power of RED systems. Finally, in Sec. VI, we conclude with a discussion on future outlooks and a brief summary.

II. THE ELECTRICAL RESPONSES OF NANOFLUIDIC SYSTEMS

The model derived in this work provides a self-consistent $I - V$ response for a nanofluidic system, comprised of a nanochannel and two larger channels connected to the infinitely large bulk reservoirs. We will demonstrate that this model reduces to three known limits and, as such, serves as a unifying model. To explain the results of this new model, we will build upon the simpler models. While we will show that the unifying model shares attributes of several models, the final result is not merely a superposition of these previous solutions.

Before proceeding with the introduction of the model and the analysis, we make one last comment about the notations. The manuscript includes a surprisingly large number of parameters, variables, subscripts, superscripts, tildes, and hats. To improve the readability, Supplemental Material [35] includes a section that details the nomenclature of this work.

A. Various systems considered in this work

Figure 2 depicts the four considered scenarios. Two of the scenarios include only the nanochannel region (one layer, denoted by 1L), while the other two account for the effects of the much larger reservoirs (three layers, denoted by 3L). Two of the scenarios assume symmetric concentrations, while the other two explicitly involve asymmetric concentrations, denoted as $C_r = 1$ and $C_r \neq 1$ systems, respectively. To summarize, the four scenarios considered in this work are as follows:

1. 1L and $C_r = 1$ [Fig. 2(a)]: One layer with symmetric concentrations.
2. 1L and $C_r \neq 1$ [Fig. 2(b)]: One layer with asymmetric concentrations.
3. 3L and $C_r = 1$ [Fig. 2(c)]: Three layers with symmetric concentrations.
4. 3L and $C_r \neq 1$ [Fig. 2(d)]: Three layers with asymmetric concentrations.

The derived expressions for the last scenario of 3L and $C_r \neq 1$ are the novelty of this work.

B. Current-voltage characteristics

The current-voltage ($I - V$) response, commonly used to characterize their electrical response, differs for all four scenarios. Each scenario and the main characteristics used

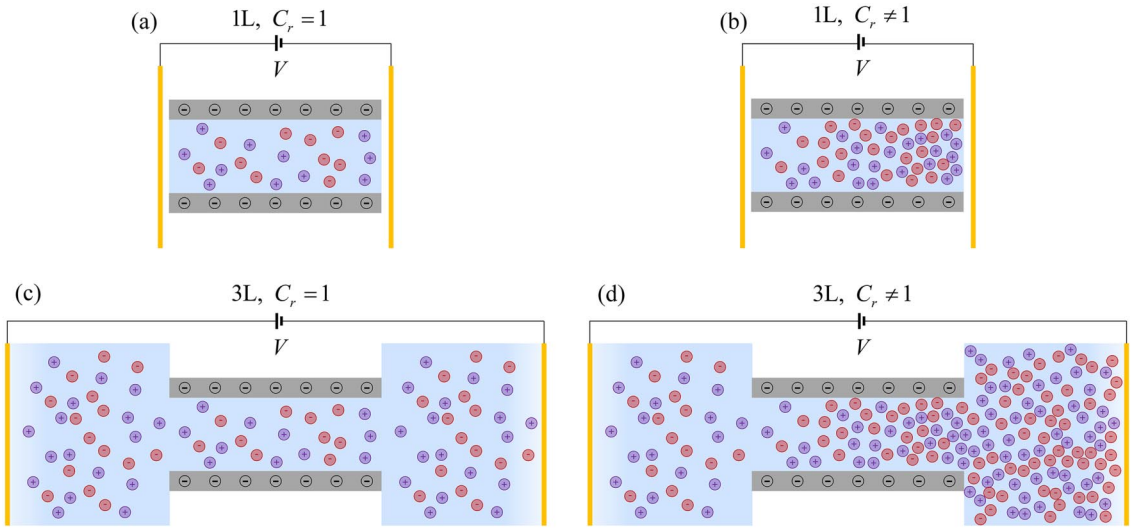

FIG. 2. Schematic representation of the four system configurations considered in this work, which either include (a,b) one layer (1L), only the charged nanochannel, or (c,d) a three-layer (3L) system, which also includes the adjoining (noncharged) microchannels. Either system can be subjected to (b,d) a concentration gradient ($C_r \neq 1$) or (a,c) no concentration gradient ($C_r = 1$).

therein require a detailed discussion. Thus, for brevity, here, we provide a brief overview of the main characteristics of the $I-V$ response so that the terminology is clear. The behavior of each characteristic will then be discussed as the need arises.

Consider the $I-V$ for symmetric concentrations ($C_r=1$). For such a symmetric system, the $I-V$ response goes through the origin [purple line in Fig. 3(a)]. At low voltages, the response is characterized by the linear Ohmic conductance, $G_{\text{Ohmic}}=I/V$, or its reciprocal, the Ohmic resistance, $R_{\text{Ohmic}}=G_{\text{Ohmic}}^{-1}=V/I$. At high voltages, the current is (diffusion-)limited such that it "almost" saturates to a limiting value known as the limiting current, I_{lim}. Two comments about the limiting current are needed. First, limiting currents are observed only in three-layered systems; one-layered systems do not exhibit limiting currents. Yet, whether or not a limiting current is to be found in the system does not vary the robustness of the analysis. Second, the main text focuses on the low-voltage Ohmic conductance. Yet, for completeness, several comments on the limiting (and over-limiting) currents are given in Supplemental Material [35].

If the concentrations are asymmetric ($C_r\neq 1$), the $I-V$ is shifted from the origin [crimson line in Fig. 3(a)], yielding two additional important intercept points: the zero-current voltage, $V_{I=0}$ (also known as open-circuit voltage, osmotic voltage [10,36], reversal voltage [37,38], or transmembrane potential [39,40]), and zero-voltage current, $I_{V=0}$ (also known as short-circuit current, osmotic current [10,36], and streaming current [41]). In this work, we focus on the responses at these two intercept points. However, in Supplemental Material [35], we demonstrate that our theory reproduces the $I-V$'s shown schematically in Fig. 3(a).

Figure 3(b) provides a brief overview of the behavior of R_{Ohmic} of the three known systems. For the 1L and $C_r=1$ scenario [dotted purple line], at high concentrations, the resistance decreases linearly with the bulk concentration, while at low concentrations, it saturates to a value determined by the surface charge density. The behavior of the 1L and $C_r\neq 1$ scenario [dotted crimson line] shows a similar qualitative behavior but with quantitative changes: depending on the value of C_r, the high-concentration response exhibits an upward or downward shift, as well as a left/right shift of the transition point from a bulk-dominated response to a surface charge-dominated response (see Ref. [42] for more details). The response of the 3L and $C_r=1$ scenario [dashed purple line] behaves differently at low concentration. Rather than saturating, it shows a continued linear increase with the decreasing concentration. It has been shown [43–45] that the additional increase of the resistance, with decreasing concentration, is due to the diminishing contribution of the nanochannel resistance and increasing contribution of the microchannels and the field focusing resistances (which are generalizations to the access resistances—the difference between field focusing and access resistances is discussed in great detail in Ref. [45]).

To summarize the knowledge gap: to date, there is no known model that predicts how $R_{\text{Ohmic}}, V_{I=0}, I_{V=0}$, the power, P, and all the remaining characteristics should behave for the 3L and $C_r\neq 1$ scenario. This work provides that response and explains the new results by leveraging the understanding from all the "simpler" scenarios. However, it should be noted, once more, that the results of the 3L and $C_r\neq 1$ scenario are not a mere superposition of the previous simpler models.

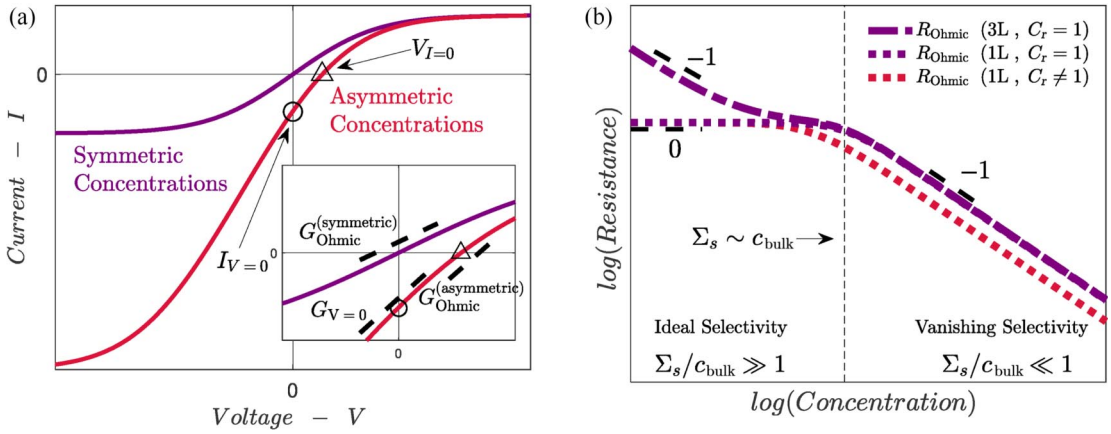

FIG. 3. (a) The current-voltage, $I-V$, response of a nanofluidic system subject to symmetric ($C_r=1$) and asymmetric ($C_r\neq 1$) concentrations, marked in purple and crimson curves, respectively. The inset shows a close-up of the origin, highlighting the two intercept points of $C_r\neq 1$: the zero-current voltage, $V_{I=0}$, and the zero-voltage current, $I_{V=0}$. The low current response is characterized by a linear resistance, R_{Ohmic}, which is reciprocal to the conductance, $G_{\text{Ohmic}}=R_{\text{Ohmic}}^{-1}$. At high voltages, the current saturates to, not necessarily symmetric, limiting currents. (b) Schematic of the resistance, R_{Ohmic}, versus the bulk concentration, c_{bulk}, for the various scenarios described in the main text.

III. MODEL

A. Geometry

Figure 4 shows the schematic of our three-layered system consisting of two microchannels (denoted as regions 1 and 3) connected by a nanochannel (denoted as region 2). For visual clarity, we have removed the electrodes at the two ends of the system that appear in Fig. 1. The geometric parameters of each region are denoted by L_k, H_k, and W_k, representing the length, height, and width, respectively, where the index $k = 1, 2, 3$ corresponds to regions 1, 2, and 3. Here, we consider the more general case in which the microchannels are not necessarily symmetric.

The coordinate system is defined such that the x axis runs along the microchannels and the nanochannel for $y = 0, z = 0$. The origin, $x = 0$, is set at the leftmost edge of the left microchannel (region 1). The cumulative lengths in the systems are defined by

$$\Delta_1 = L_1, \qquad \Delta_2 = \Delta_1 + L_2, \qquad \Delta_3 = \Delta_2 + L_3. \quad (2)$$

The microchannel-nanochannel interfaces at $x = \Delta_1$, and $x = \Delta_2$ (regions marked in blue in Fig. 4) are explicitly utilized in the boundary conditions used in Supplemental Material [35].

Two last comments are needed. First, we have represented the nanochannel geometry as having a rectangular cross section. However, this need not be the case, and we can consider the nanochannel to be of arbitrary cross section. As discussed in our Supplemental Material [35] and thoroughly in Ref. [43], the transport problem within the nanochannel is reduced to the solution of an effective one-dimensional (1D) profile, making the cross-sectional shape irrelevant to the derivation. Second, in this work, we consider the simplest scenario of a uniform surface charge distribution. Even for this "simple" scenario, the mathematical derivation and analysis are remarkably difficult and novel. The effects of a nonuniform surface charge distribution (such as bipolar [16,46–54] or tripolar [55,56] channels) subject to $C_r \neq 1$ are left for future work.

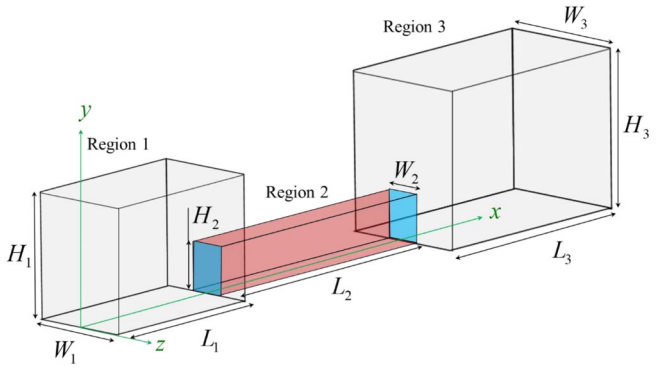

FIG. 4. A 3D schematic plot of the three-layer (micro-nano-micro channels) system, where the microchannels (regions 1 and 3) are not necessarily geometrically symmetric. The coordinate system is given in green, where the x axis line (i.e., $y = 0, z = 0$) runs along the center of the microchannels and nanochannel (region 2). The interfaces of the microchannels and nanochannels are marked in blue, while the nanochannel is marked in red.

B. Governing equations

To accurately characterize ion transport processes in ion-selective materials, we solve the continuum-based advectionless steady-state Poisson-Nernst-Planck (PNP) equations. We assume that the system is filled with a KCl(-like) saline solution with equal diffusion coefficients, $D_\pm = D$, and symmetric valences, $z_\pm = \pm z$. For simplicity, we take the valency to be unity, $z = 1$. Then, the PNP equations can be written as

$$-\nabla \cdot \mathbf{j}_\pm = \nabla \cdot \left(D\nabla c_+ \pm z\frac{DF}{\Re T} c_+ \nabla\phi \right) = 0, \quad (3)$$

$$\varepsilon_0 \varepsilon_r \nabla^2 \phi = -\rho_e = -F(zc_+ - zc_- - \Sigma_s \delta_{2k}), \quad (4)$$

where F is the Faraday constant, $\Re$ is the universal gas constant, T is the absolute temperature, and ε_0 and ε_r are the permittivity of vacuum and the relative permittivity of the solution, respectively. In steady-state, the Nernst-Planck equations [Eq. (3)] are reduced to the divergence of the flux density vectors, $\mathbf{j}_\pm$, which determine the distribution of the positive and negative ion concentrations, c_+ and c_-, respectively. The Poisson equation, Eq. (4), which determines the electric potential distribution, ϕ, depends on the space charge density, ρ_e, which has been written in a general manner such that it holds for all three regions. Herein, δ_{2k} is Kronecker's delta when $k = 1, 2, 3$. In regions 1 and 3, the space charge density is comprised only of the two concentrations. In contrast, in region 2, an additional term exists. This term is the effective excess counterion concentration, $\Sigma_s > 0$ (called "fixed charges" in Teorell-Meyer-Sievers theory [57–59]), accounting for the (negative) surface charge density, σ_s.

In region 2, the surface charge density, σ_s, is a key parameter (this is in contrast to regions 1 and 3, where σ_s is negligible). If one considers a cross-sectional averaging procedure [35], which is valid so long as $L_2 \gg A^{1/2}$, then σ_s gives rise to an excess average counterion concentration Σ_s. For a straight, nontortuous nanochannel, the $\Sigma_s - \sigma_s$ relation is straightforward [45]

$$\Sigma_s = -\frac{\sigma_s \mathcal{P}}{FA}, \quad (5)$$

where $\mathcal{P}$ is the perimeter and A is the cross-sectional area. Note that from this relation, one can experimentally measure σ_s [by extracting Σ_s from conductance-concentration experiments, Fig. 3(b)]. For nanoporous membrane

systems, Σ_s is typically the empirically measured property (and σ_s cannot be extracted directly) [60]. Regardless, in both systems, Σ_s is treated as a fixed concentration that is a material property that is independent of the bulk concentration. Since Σ_s is the only important property that must be accounted for in both systems, nanoporous materials and nanochannels behave precisely the same. Thus, we can use either terminology (membrane or nanochannel) interchangeably.

Note that in principle, σ_s varies not only with the material properties but also with the electrolyte properties. It has been demonstrated [61–63] that if the material and electrolyte interact with each other, the surface charge density is regulated such that σ_s depends on several parameters, including the bulk concentration and bulk pH. However, in all these analytical models, it was assumed that the system was subjected to symmetric concentrations, and to date, there is no model that accounts for surface charge regulation with asymmetric concentrations. This is because the introduction of surface charge regulation with asymmetric concentration will introduce substantial mathematical complications. Thus, in this work, we focus on the much simpler case where the surface charge density is a nonvarying property (i.e., no charge regulation) and leave the issue of surface charge regulation combined with asymmetric concentration for future work. Similarly, the inclusion of advection also introduces substantial mathematical complexities that cannot be addressed here. To better understand these complexities, the interested reader is referred to our recent work [54] or Supplemental Material [35], which discuss these issues thoroughly. We merely note that once advection is accounted for, one can no longer use the cross-sectional averaging approach, since this approach yields incorrect results (see Ref. [64], which discusses the downfall of the uniform potential model upon the inclusion of advection).

The system is subjected to a combined concentration gradient (i.e., different bulk concentrations) and an electric potential drop of V

$$c_\pm(x=0)=c_{\text{left}},\quad c_\pm(x=\Delta_3)=c_{\text{right}},\qquad \phi(x=0)=V,\quad \phi(x=\Delta_3)=0. \tag{6}$$

Note that the potential drop has been defined as positive, $V>0$, from left to right (along the x axis), leading to a positive electrical current, $I>0$. When solving a two-dimensional (2D) or three-dimensional (3D) problem, additional no-flux BCs are required at the remaining impermeable surfaces (see Supplemental Material [35]).

Before proceeding with our analysis, one last comment is needed regarding the derivation process. The model in this work explicitly assumes that the system is locally (and thus globally) electroneutral, where $\rho_e=0$. Electroneutrality occurs when the left-hand side of Eq. (4) is negligible. This happens when the Debye length, defined as $\lambda_D=\sqrt{\varepsilon_0\varepsilon_r\Re T/2F^2c_{\text{bulk}}}$, where c_{bulk} is either c_{left} or c_{right}, is substantially smaller than the longitudinal lengths in this system—in this case, all of the L's, and in particular L_2. It is essential to note that the Debye length also determines the degree of selectivity of the systems. In Ref. [65,66], we showed that the nondimensional Σ_s (normalized by either of the bulk concentrations, denoted here as c_{bulk}) yields that $\Sigma_s/c_{\text{bulk}}\sim|\Sigma_s|(\lambda_D/H_2)^2$ (see Ref. [65] for more details regarding the remaining dimensionalizations). If $\lambda_D/H_2\ll1$, then one finds that the effects of the surface charge are negligible and the system is vanishingly selective. In the other limit, $\lambda_D/H_2\gg1$, the effects of the space charge are immensely important, and the system is highly selective. In Fig. 5 of Ref. [66], we demonstrated that the excess counterion concentration (Σ_s) formulation and surface charge density (σ_s) formulation yield the same results. Regardless of the ratio $\lambda_D/H_2\gg1$, in the derivation process, we will assume that $\lambda_D/L_2\ll1$ (in other words, we also assume that $L_2/H_2\gg1$).

Finally, in this work, rather than considering the two ionic fluxes (j_+ and j_-) given in Eq. (3), we consider their difference and their sum. These yield the salt flux and electrical current density, given by $j=j_++j_-$ and $i=F(j_+-j_-)$, respectively, which have different units ($\text{mol}/\text{m}^2\text{s}$ and A/m^2, respectively) [43,67,68]. In this work, we will often consider the currents, I and J, and not the current densities, i and j. These two (as well as all quantities and their densities) are trivially related through the cross-sectional area, $I=iA$, so long as the current density is assumed to be uniform across the cross section. In 3D, $A=H_2W_2$ is a rectangle, while in 2D $A=H_2$. Note that I and J can also be reduced to 2D (if $W_{1,3}=W_2$ or $H_{1,3}=H_2$).

C. Two master equations: The $i-V$ and $i-j$ relations

In the main text, we shall focus on the presentation and analysis of the two master equations derived (in detail) in Supplemental Material [35], which, for the first time, account for the microchannels and concentration asymmetry (3L and $C_r\neq1$). Before introducing the two master equations, it is worthwhile to first introduce several intermediate expressions on which these equations depend.

These intermediate expressions are the interfacial concentrations located at $x=\Delta_1,\Delta_2$

$$\bar{c}_1=c_{\text{left}}-\frac{J\Sigma R_1}{2\rho_{\text{res}}D},\qquad \bar{c}_3=c_{\text{right}}+\frac{J\Sigma R_3}{2\rho_{\text{res}}D}. \tag{7}$$

Here $\rho_{\text{res}}=\Re T/F^2Dc_{\text{bulk}}$ is the resistivity. These interfacial concentrations depend on the local geometry through the R functions

$$R_{k=1,2,3} = \rho_{\mathrm{res}} \frac{L_k}{W_k H_k}, \qquad R_{\mathrm{FF},k=1,3} = 2\rho_{\mathrm{res}} \bar{f}_k,$$
$$\Sigma R_{k=1,3} = R_k + R_{\mathrm{FF},k}. \tag{8}$$

These functions are precursors to the electrical resistances that will be provided later. In the remainder, we denote all interfacial quantities with an overbar.

In principle, each of the electrical resistances can be divided into two contributions. The geometric contribution multiplied by ρ_{res}—these are the R functions—and an additional contribution accounting for interfacial phenomena [which will be introduced later and depends on Eq. (7) and the soon-to-be-introduced Eq. (9)]. When $C_r = 1$, the microchannel resistances are given precisely by Eq. (8), while the nanochannel resistance requires some modification (see Ref. [43] for a detailed derivation and discussion of the $C_r = 1$ result).

Equation (8) provides the geometric contribution of the system's five resistances. Three of these resistances, $R_{k=1,2,3}$, are the cuboidal Ohmic resistances of each region, given by the ratio of the region's length to its cross-sectional area, multiplied by ρ_{res}. The two remaining resistances, $R_{\mathrm{FF},k=1,3}$, are termed the field-focusing resistances. The expressions of the $\bar{f}_{k=1,3}$ functions are long and tedious, and therefore are provided in Supplemental Material [35]. The field-focusing resistance is related to what is known within the nanofluidic community as access resistance. Access resistance, derived first by Hall [69], accounts for the focusing of electric field lines of a single isolated circular pore in an infinite reservoir. As such, the expression for this resistance depends only on one characteristic length—the radius of the pore. In contrast, $R_{\mathrm{FF},k}$ depends on the finite size of the microchannels (H_k, W_k and L_k) and on the nanochannel geometry (H_2 and W_2). As such, the field-focusing resistance serves as a generalization of the access resistance. This generalization—extending $R_{\mathrm{FF},k}$ from a rectangular to an arbitrary nanochannel geometry—is discussed thoroughly in Ref. [45]. Note that in regions 1 and 3, there is a dual contribution of the cuboidal Ohmic resistor and the field-focusing resistor. For brevity, we termed this combined resistance as ΣR_k.

The third intermediate functions are

$$\bar{S}_1 = \frac{1}{2}\bar{c}_1 \sqrt{\left(\frac{\Sigma_s}{\bar{c}_1}\right)^2 + 4}, \qquad \bar{S}_3 = \frac{1}{2}\bar{c}_3 \sqrt{\left(\frac{\Sigma_s}{\bar{c}_3}\right)^2 + 4}. \tag{9}$$

These functions account for the Donnan potential drop (due to Σ_s) at the two interfaces located at $x = \Delta_1, \Delta_2$. These functions depend on the two interfacial concentrations $\bar{c}_{1,3}$ [Eq. (7)] and on Σ_s [Eq. (5)]. The ratios $\Sigma_s/\bar{c}_1$ and $\Sigma_s/\bar{c}_3$ (and later $\Sigma_s/c_{\mathrm{left}}$ and $\Sigma_s/c_{\mathrm{right}}$) are perhaps the most important nondimensional numbers in the system. For example, if $\Sigma_s/\bar{c}_1 \ll 1$, then the effects of the Σ_s (which represents the effects of the surface charge) are almost negligible, and the response is determined by the bulk concentration. This scenario corresponds to the case where the Donnan potential jump/drop is negligible. If $\Sigma_s/\bar{c}_1 \gg 1$, the response is determined by the surface charge and is independent of the bulk properties. This scenario corresponds to the case where the Donnan potential jumps are substantial. Since we have several nondimensional numbers ratios, the overall response is determined not by one but rather by the interplay of these numbers. We will later demonstrate that these ratios determine the change in the behavior of all the key transport characteristics. We will do so by keeping Σ_s constant while varying c_{left} for several values of $C_r = c_{\mathrm{right}}/c_{\mathrm{left}}$.

Finally, we are ready to introduce the two master equations. The first equation is the highly desirable relation relating the electrical current density and the voltage. The voltage drop across all three layers and the Donnan jumps is given by

$$V(i,j) = V_{\mathrm{th}}\left[\frac{i}{Fj}\ln\left(\frac{\bar{c}_3}{\bar{c}_1}C_r^{-1}\right) + \ln\frac{\bar{c}_3}{\bar{c}_1} - \ln\frac{\Sigma_s + 2\bar{S}_3}{\Sigma_s + 2\bar{S}_1} + 2\frac{\bar{S}_3 - \bar{S}_1}{\Sigma_s} + \frac{jAR_2}{D\Sigma_s\rho_{\mathrm{res}}}\right], \tag{10}$$

where $V_{\mathrm{th}} = \Re T/F$ is the thermal voltage. The first two terms can be associated with the potential drops across regions 1 and 3. The middle term accounts for the two Donnan potential jumps (at $x = \Delta_1, \Delta_2$). The final two terms account for the potential drop across the nanochannel. One can already observe that the notation of $i - V$ drastically oversimplifies the situation, as the potential drop also depends on the salt current density, j, such that the notation $V(i,j)$ is perhaps the most fitting. Yet, one should remember that at the end of the day, experimentalists measure $i - V$'s. In the following, we use the notations $i - V$ and $V(i,j)$ interchangeably.

Since we have charged species, we have two fluxes, j_+ and j_-, which can be translated into j and i. Similar to how j_+ and j_- are interrelated, so too are j and i. Thus, the second equation is the equation that relates j and i–this is the salt flux-electrical current density ($i - j$) relation

$$\frac{\Sigma_s i}{2Fj}\ln\left(\frac{i\Sigma_s - 2jF\bar{S}_3}{i\Sigma_s - 2jF\bar{S}_1}\right) + (\bar{S}_3 - \bar{S}_1) + \frac{jAR_2}{2D\rho_{\mathrm{res}}} = 0. \tag{11}$$

As can be observed, this $i - j$ relation is nonlinear. The first and second terms account for the changes in regions 1 and 3 and the Donnan potential, respectively. The last term accounts for the nanochannel.

Equations (10) and (11) form a closed set of equations that fully determine the electric response of the system, which depend on the geometry (through the $\bar{c}_{1,3}$ and $\bar{S}_{1,3}$

functions) and the surface charge [through Σ_s, Eq. (5)]. Since these equations are nonlinear, in general, they need to be solved numerically.

In this work, we focus on the two crossover points, $I = 0$ and $V = 0$. We focus on the zero electrical current, $I = 0$, state because we can derive simple and tractable expressions for the most important transport characteristics of the system (something that cannot be done for $V = 0$). Importantly, these new expressions can be reduced to the expected limits of the various scenarios shown in Fig. 2, while providing much information on the zero-voltage state. However, for the sake of completeness, in Supplemental Material [35], we demonstrate that governing equations [Eqs. (10) and (11)] capture the complete $i - V$ (including the limiting currents not discussed in this work).

All theoretical predictions in this work are verified by nonapproximated numerical simulations of the PNP equations (the details of the simulations can be found in Supplemental Material [35]). For the sake of brevity, in the following, we will no longer remark on the remarkable correspondence of the theoretical results with the nonapproximated numerical simulations (given by markers throughout this work).

IV. ZERO ELECTRIC CURRENT RESPONSE, $I = 0$

The zero electrical current, $I = 0$, state is of utmost importance. In this state, one can find several meaningful transport characteristics, including the zero-electrical current voltage, $\hat{V}_{I=0}$, the equilibrium transport number, τ, and the Ohmic resistance, $R_{\text{Ohmic}} = \hat{R}_{I=0}$. Most of these characteristics also depend on the salt current at zero-electrical current, $\hat{J}_{I=0}$. Here, the notation with a hat denotes properties at the $I = 0$ condition, such that properties with a combination of overbar and a hat are interfacial properties at the $I = 0$ condition.

A. Mathematical simplification

Inserting $I = 0$ into the $i - j$ relation [Eq. (11)], provides a relatively simple equation for the salt current at zero electric current, $\hat{J}_{I=0}$

$$2D(\hat{\bar{S}}_3 - \hat{\bar{S}}_1) + \hat{J}_{I=0}R_2/\rho_{\text{res}} = 0, \tag{12}$$

when $J = \hat{J}_{I=0}$ is inserted into Eqs. (7)–(9) such that $\hat{\bar{S}}_{k=1,3} = \sqrt{\frac{1}{4}\Sigma_s^2 + \hat{\bar{c}}_{k=1,3}^2}$ when $\hat{\bar{c}}_1 = c_{\text{left}} - \hat{J}_{I=0}\Sigma R_1/(2\rho_{\text{res}}D)$ and $\hat{\bar{c}}_3 = c_{\text{right}} + \hat{J}_{I=0}\Sigma R_3/(2\rho_{\text{res}}D)$. Then, it can be shown that Eq. (12) is effectively a fourth-order polynomial for $\hat{J}_{I=0}$. Given the long expressions for each of the coefficients of the polynomial, the expressions for the roots are not tractable. As such, we treat Eq. (12) as a transcendental equation that needs to be solved numerically (the numerical procedure is detailed in Supplemental Material [35]). In the remainder, we will treat $\hat{J}_{I=0}$ as a known function, such that any function that depends on $\hat{J}_{I=0}$ can also be treated as known.

We now insert $I = 0$ into Eq. (10), which yields the voltage at zero current

$$\hat{V}_{I=0} = V_{I=0} = V_{\text{th}}\left(-\ln\frac{\hat{\bar{c}}_1}{\hat{\bar{c}}_3} + \ln\frac{\Sigma_s + 2\hat{\bar{S}}_1}{\Sigma_s + 2\hat{\bar{S}}_3}\right). \tag{13}$$

We retain the subscript $I = 0$, making the overhead hat notation somewhat redundant, and use $V_{I=0}$ and $\hat{V}_{I=0}$ interchangeably.

To simplify Eqs. (10) and (11), we leverage that i and are related through the (nondimensional) counterion transport number τ, defined as [43,67]

$$\tau = \frac{j_+}{j_+ - j_-} = \frac{1}{2} + \frac{1}{2}\frac{Fj}{i} = \frac{1}{2} + \Delta\tau. \tag{14}$$

The transport number (discussed more thoroughly in Supplemental Material [35]) is a major transport characteristic of a permselective system, and, depending on the degree of permselectivity, it varies between $\frac{1}{2}$ (vanishing permselectivity) and 1 (ideal permselectivity). Note that, except for the symmetric scenario (where $C_r = 1$ and $\hat{J}_{I=0} \triangleq 0$), the ratio J/I diverges at $I = 0$. However, if one uses the following modification for the asymmetric scenario ($C_r \neq 1$) [42,65,70]

$$J = \hat{J}_{I=0} + 2I\Delta\tau/F, \tag{15}$$

the divergence is removed. Inserting Eq. (15) into Eq. (11) transforms the $i - j$ relation to a $i - \Delta\tau$ relation. We then take the Taylor series of the $i - \Delta\tau$ relation around $I = 0$ (or $i = 0$) and require that both leading-order terms (zeroth- and first-order) be zero. The zeroth-order term reproduces Eq. (12) and does not yield new information. However, the first-order term yields an expression from which the transport number can be calculated

$$\Delta\hat{\tau} = \frac{\rho_{\text{res}}D\Sigma_s}{2\hat{J}_{I=0}}\left(\frac{\hat{\bar{c}}_1}{\hat{\bar{S}}_1}\Sigma R_1 + R_2 + \frac{\hat{\bar{c}}_3}{\hat{\bar{S}}_3}\Sigma R_3\right)^{-1}\ln\left(\frac{\hat{\bar{S}}_1}{\hat{\bar{S}}_3}\right). \tag{16}$$

Inserting Eqs. (15) and (16) into Eq. (10), and taking the Taylor series around $I = 0$, reduces Eq. (10), to first order, to a shifted Ohm's law

$$V_{I\ll 1} = IR_{\text{Ohmic}} + \hat{V}_{I=0}, \tag{17}$$

where

$$R_{\mathrm{Ohmic}} = \frac{2c_{\mathrm{bulk}}\Delta\hat{\tau}}{\Sigma_s}\left(\frac{\hat{\bar{S}}_1}{\hat{\bar{c}}_1}\Sigma R_1 + R_2 + \frac{\hat{\bar{S}}_3}{\hat{\bar{c}}_3}\Sigma R_3\right) + \frac{V_{\mathrm{th}}}{F\hat{J}_{I=0}}\ln\left(\frac{1}{C_r}\frac{\hat{\bar{c}}_3}{\hat{\bar{c}}_1}\right), \tag{18}$$

is the total electrical resistance. Note that both $\Delta\hat{\tau}$ and R_{Ohmic} depend on the "geometric" resistances (given by the R functions) multiplied by interfacial properties, such that the electric resistances of each region are given by nontrivially complicated expressions, which also depend on the numerically calculated $\hat{J}_{I=0}$.

To keep the main text as short as possible, the reduction of all the transport characteristics ($\hat{J}_{I=0}, \hat{V}_{I=0}, \Delta\hat{\tau}$ and R_{Ohmic}), derived in Sec. IV A, to the three previous models depicted in Fig. 2, is provided in Supplemental Material [35].

B. Onsager reciprocity

In this section, we have reduced the governing equations [Eqs. (10) and (11)] to Eqs. (15) and (17). Equation (17) can be rewritten as

$$I = \frac{1}{R_{\mathrm{Ohmic}}}V_{I\ll 1} - \frac{\hat{V}_{I=0}}{R_{\mathrm{Ohmic}}}. \tag{19}$$

Inserting this into Eq. (15) yields

$$J = \frac{2\Delta\tau}{FR_{\mathrm{Ohmic}}}V_{I\ll 1} + \left(\hat{J}_{I=0} - \frac{2\Delta\tau}{F}\frac{\hat{V}_{I=0}}{R_{\mathrm{Ohmic}}}\right). \tag{20}$$

We have written Eqs. (19) and (20) in the following manner. On the left-hand side, one has the fluxes (J and I), while on the right-hand side, one has the driving forces multiplied by the corresponding transport coefficients "mobilities/conductances." Here, the driving forces are the applied potential, $V_{I\ll 1}$, and the chemical potential difference, which we will denote as $\Delta\mu = \mu_{\mathrm{right}} - \mu_{\mathrm{left}} = \Re T \ln C_r^{-1}$.

Ideally, one would like to write these two equations to have the form of Onsager's reciprocal matrix, such that

$$\begin{pmatrix} I \\ J \end{pmatrix} = \begin{pmatrix} \chi_{VV} & \chi_{V\Delta\mu} \\ \chi_{\Delta\mu V} & \chi_{\Delta\mu\Delta\mu} \end{pmatrix}\begin{pmatrix} V \\ \Delta\mu \end{pmatrix}, \tag{21}$$

where each one of the χ terms can supposedly be identified in (19) and (20). Based on Onsager's theorem, a system close to equilibrium should exhibit reciprocity, specifically $\chi_{V\Delta\mu} = \chi_{\Delta\mu V}$. As we will show, $\chi_{V\Delta\mu} = \chi_{\Delta\mu V}$ does not generally hold.

Before going into the proof, we provide an intuitive explanation of why this should be the case. Equations (19) and (20) represent the simplified master equations after we linearized the two master equations [Eqs. (10) and (11)]. In general, the two master equations are nonlinear and coupled, and thus cannot be written in the form of Eq. (21). Perhaps this should not be a surprise, since the system is far from quasiequilibrium, where equilibrium is the state of zero fluxes, and Onsager reciprocity requires the system to be near a thermodynamic equilibrium (implying no fluxes). However, in this system, there are always fluxes—which are usually related in a nonlinear manner to their driving forces [Eqs. (10) and (11)]. In a quasiequilibrium state, one is not far from the origin. However, here the $I-V$ does not cross the origin—and thus, the system is always far away from (quasi)equilibrium.

Since $\hat{J}_{I=0}$ is not known analytically for the 3L system, the proof that the system is far away from equilibrium is mathematically involved. This can be bypassed by considering the simpler 1L scenario, where all the transport characteristics are given by tractable expressions. The reduction from the 3L solution to 1L is given in Supplemental Material [35] (an alternative and direct derivation can be found in Ref. [42]). Note that when the microchannels are ignored, the S functions take the simpler form $\bar{S}_1 = \sqrt{\frac{1}{4}\Sigma_s^2 + c_{\mathrm{left}}^2}$ and $\bar{S}_3 = \sqrt{\frac{1}{4}\Sigma_s^2 + c_{\mathrm{right}}^2}$. Then, the characteristics are given by

$$\hat{j}_{I=0} = \frac{\hat{J}_{I=0}}{A} = 2D(\bar{S}_1 - \bar{S}_3)\frac{1}{L_2}, \tag{22}$$

$$\hat{V}_{I=0} = V_{\mathrm{th}}\left[-\ln\left(\frac{1}{C_r}\right) + \ln\left(\frac{\Sigma_s + 2\bar{S}_1}{\Sigma_s + 2\bar{S}_3}\right)\right], \tag{23}$$

$$\Delta\hat{\tau} = \frac{D\Sigma_s}{2L_2\hat{j}_{I=0}}\ln\left(\frac{\bar{S}_1}{\bar{S}_3}\right), \tag{24}$$

$$R_{\mathrm{Ohmic}} = \frac{\Re T}{F^2 D}\frac{\ln(\bar{S}_1/\bar{S}_3)}{2(\bar{S}_1 - \bar{S}_3)}\frac{L_2}{A}. \tag{25}$$

We can insert these into Eqs. (19) and (20), from which we find the off-diagonal terms. The $\chi_{\Delta\mu V}$ term from Eq. (20) is straightforward

$$\chi_{\Delta\mu V} = \frac{2\Delta\tau}{FR_{\mathrm{Ohmic}}} = \frac{\Sigma_s AD}{V_{th}L_2}. \tag{26}$$

The $\chi_{V\Delta\mu}$ term from Eq. (19) requires an additional division by $\Delta\mu = \Re T \ln C_r^{-1}$

$$\chi_{V\Delta\mu} = \frac{\hat{V}_{I=0}}{R_{\mathrm{Ohmic}}\Re T \ln C_r^{-1}} = \frac{2D}{V_{th}\ln C_r^{-1}}\frac{A}{L_2}\frac{(\bar{S}_1 - \bar{S}_3)}{\ln(\bar{S}_1/\bar{S}_3)}\ln\left(\frac{\Sigma_s + 2\bar{S}_1}{\Sigma_s + 2\bar{S}_3}C_r\right). \tag{27}$$

These two terms [Eqs. (26) and (27)] are entirely different, further proving that, in general, Onsager reciprocity fails. However, if one considers two bulk concentrations that are almost symmetric, such that $C_r = 1 + \Delta c/c_{\text{left}}$ and $\Delta c/c_{\text{left}} \ll 1$, then the Taylor series of Eq. (27) yields the expected result, where it can be shown that the ratio $\chi_{V\Delta\mu} = \chi_{\Delta\mu V}$. However, the limit $\Delta c/c_{\text{left}} \ll 1$ is uninteresting from the point of RED, where large C_r (and thus large $\Delta c/c_{\text{left}} \gg 1$) are highly desirable.

It is also interesting to note that $\hat{J}_{I=0}, \hat{V}_{I=0}, \Delta\hat{\tau}$, and R_{Ohmic} do not explicitly depend on $\Re T \ln C_r^{-1}$ or on the gradient of the chemical potential at the two ends of the system. Rather, they depend on complicated functions of c_{left} or c_{right} through the $\bar{S}_{1,3}$ functions (and the nonlinear dependency of these functions on these concentrations), which represent the far-from-equilibrium Donnan potential drop.

It can also be noted that $\chi_{VV}(c_{\text{left}}, c_{\text{right}}) = 1/R_{\text{Ohmic}}$ is a (complicated) function of c_{left} and c_{right} but not of $\Re T \ln C_r^{-1}$ or Δc—this can readily be observed in Eq. (25). However, in the limit $\Delta c/c_{\text{left}} \ll 1, \chi_{VV}$ can be written as

$$\chi_{VV} = \frac{ADF}{L_2 V_{th}} \left(\sqrt{4c_{\text{left}}^2 + \Sigma_s^2} + \frac{2c_{\text{left}}\Delta c}{\sqrt{4c_{\text{left}}^2 + \Sigma_s^2}} \right). \quad (28)$$

It can be noted that the first term is the classical Ohmic conductance of a nanochannel subjected to symmetric concentrations, while the second term is the additional contribution of the asymmetry of the concentration. Here, it can be noted that $\chi_{VV} \sim \Delta c$. However, this would result in $I = \chi_{VV} V \sim \Delta c V$. Such a nonlinear cross term should not appear in a linear formulation. It can also be noted that, like the other terms considered thus far, the bracketed terms in Eq. (20) also do not reduce to a simple term that depends on Δc. Rather, it is a complicated function of c_{left} and c_{right}.

Since this model corresponds to the (advection-less) TMS model, also known as the (advection-less) uniform-potential model, it calls into question the results of the advection uniform-potential model, which provides a 3×3 Onsager matrix that also accounts for pressure. If the reduced 2×2 model is incorrect, then so is the 3×3 matrix. The only way to find the correct 2×2 matrix (without pressure/advection) or 3×3 matrix (with pressure and advection) is to consider the space charge model of the PNP-Stokes (PNP-S) equations. However, there, the matrix components are given in terms of double or triple integrals [71,72] that, without additional assumptions [64], need to be evaluated numerically from the solution of the PNP-S equations that do not necessarily account for longitudinal changes in a self-consistent manner. Regardless, this issue should be explored in future work.

C. Results

In this section, we present the results for the four scenarios shown in Fig. 2 for three different ratios $C_r = 10^{-1}, 1, 10$. The comparison includes both 1D and 2D systems and their respective characteristics. In 1D, a 1L system is characterized by L_2, while a 3L is characterized by all three $L_{1,2,3}$. In 2D, the 1L system is additionally characterized by H_2, while for 3L, one has three additional heights $H_{1,2,3}$. In principle, all six lengths and heights can be different. For our comparison, we kept L_2 the same for all scenarios. Then, for simplicity, we set $L_1 = L_3$, and we set these to be equal to the selected L_2. For 3L, the microchannel heights were set to be equal, $H_1 = H_3$. Then, in 1D we set $H_2 = H_1$, while in 2D we set $H_2 = H_1/500$. We found it beneficial to compare the 1L systems to the 3L-1D and 3L-2D scenarios by playing with the height of the 1L system $H_2^{(1L)}$. In the $I = 0$ section, we used $H_2^{(1L)} = H_1$, while in the $V = 0$ section, we found it useful to consider both $H_2^{(1L)} = H_1$ and $H_2^{(1L)} = H_1/500$. To ensure clarity, in the $V = 0$ section, we specify, at the beginning of each subsection, which value was used.

Due to the abundance of lengths/heights, there are several ways to compare the fluxes (and their densities) and the resistances (and their densities). We have chosen to plot the 1D $\hat{j}_{I=0}$ density (and not the height-dependent flux/current, $\hat{J}_{I=0} = \hat{j}_{I=0} H_2$), while plotting the 2D R_{Ohmic} (and not the 1D resistance density).

Finally, to improve the visibility of the plots and reduce unnecessary clutter, we plot only simulations of our new three-layer model subjected to asymmetric concentrations (3L and $C_r \neq 1$). The simulations for the remaining scenarios (and their appropriate verifications) can be found in Refs. [42,43,65,70]. Second, in all the plots, it is difficult to discern the difference between the heterogeneous 3L-2D scenario, which is mostly dominated by the nanochannel, and the 1L-1D (nanochannel-only) response. To address this, in each figure, we provide the ratio of these two solutions in the inset and show that, except for R_{Ohmic}, this ratio is very close to unity.

1. Zero-current salt current density, $\hat{j}_{I=0}$

Figure 5(a) demonstrates that $\hat{j}_{I=0}$ changes its sign when C_r crosses unity. This is expected as $\hat{j}_{I=0}$ is always directed from the higher bulk concentration to the lower bulk concentration (and when C_r crosses unity, the direction of the flux is reversed). It can be observed that as c_{left} and C_r are increased, the absolute value of the flux increases. Also, the response varies with the dimensionality (1D or 2D) of the system. In a 2D system, the response is mostly, but not always, dominated by the nanochannel, while in 1D, the microchannels are almost always of the same order of magnitude as the nanochannel, such that the high

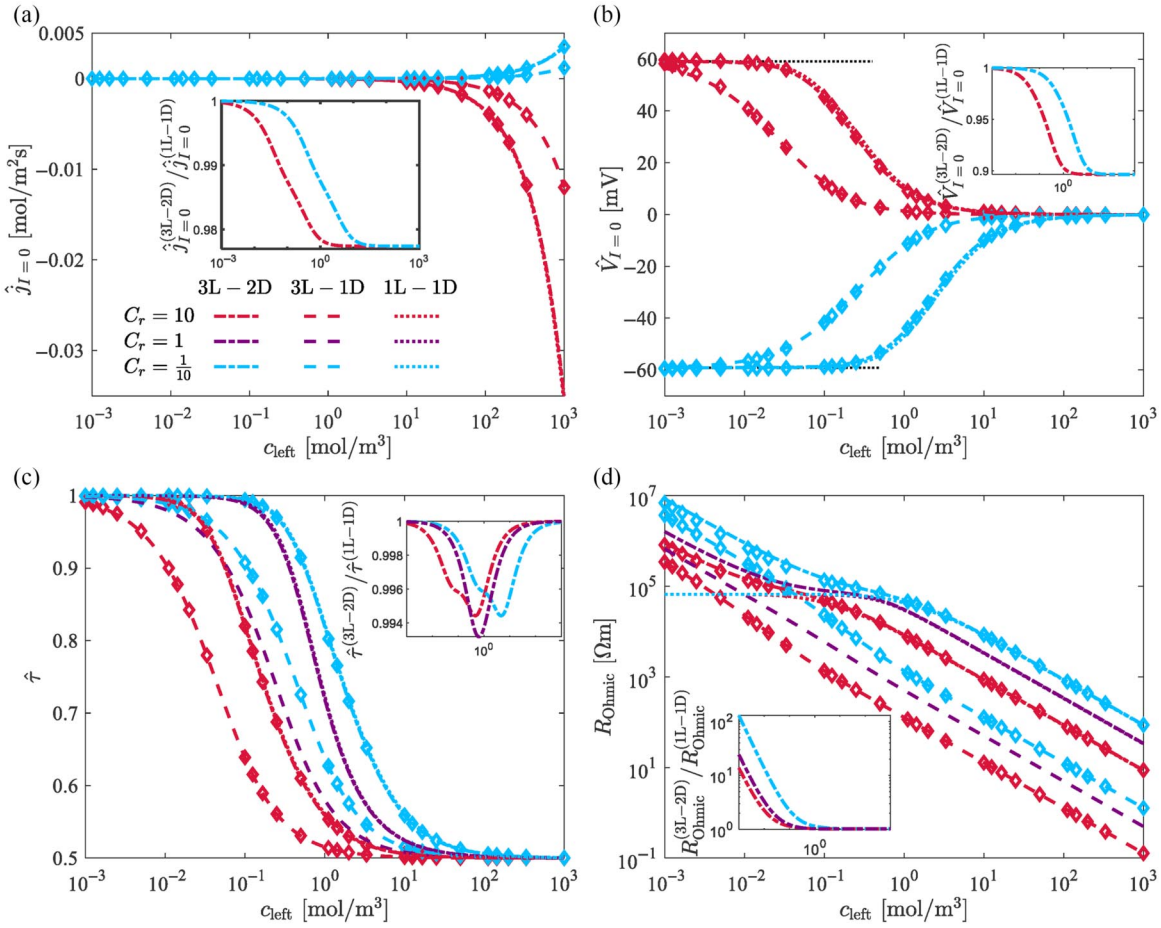

FIG. 5. Transport characteristics of a nanofluidic system versus the left bulk concentration c_{left} for several different values of $C_r = c_{\text{right}}/c_{\text{left}}$: (a) the 1D zero-current salt current density, $\hat{j}_{I=0}$, (b) the zero-current voltage, $\hat{V}_{I=0}$, (c) the transport number, $\hat{\tau}$, and (d) the 2D Ohmic resistance, R_{Ohmic}. COSMOL simulations are denoted by diamond markers, and all insets depict the ratio of the 2D three-layer solution to the 1D one-layer (nanochannel-only) solution. The geometric details are given in Supplemental Material [35]. The dotted black lines in (b) are the ideal-selective limit given by Eq. (29).

concentration resistance of the microchannel is relatively higher, leading to lower fluxes.

2. Zero-current voltage, $\hat{V}_{I=0}$

From this point forward, our analysis demonstrates that the response of all the transport characteristics varies with the two nondimensional numbers Σ_s/c_{left} and $\Sigma_s/c_{\text{right}}$. In particular, we will be interested in the limits where they are either very small or very large. These two numbers alone determine if the system is vanishingly selective or highly/ideally-selective.

Figure 5(b) presents the behavior of $\hat{V}_{I=0}$ versus the bulk concentration. It can be observed that the low-concentration $[\Sigma_s \gg \max(c_{\text{left}}, c_{\text{right}})]$ solution converges to the ideal-selective limit

$$\hat{V}_{I=0}^{(\text{ideal-selectivity})} = \hat{V}_{I=0}^{[\Sigma_s \gg \max(c_{\text{left}}, c_{\text{right}})]} = V_{\text{th}} \ln C_r, \quad (29)$$

wherein the values for $C_r = 10$ and $C_r = 10^{-1}$ have identical values but opposite signs [dotted black lines in Fig. 5(b)]. Here, we have demonstrated the convergence of $\hat{V}_{I=0}$ to Eq. (29) graphically (however, the convergence can also be shown mathematically by taking the appropriate limit [42]—we leave this to the reader).

At higher (or intermediate) concentrations, the absolute values of $\hat{V}_{I=0}$ for $C_r = 10$ and $C_r = 10^{-1}$ are not the same, indicating that the response is not just a function of and c_{right} but also depends on the geometry. This can be expected since $\hat{V}_{I=0}$ depends on the $\hat{\bar{S}}$ functions and on $\hat{j}_{I=0}$, which are functions of these parameters. It can be noted that the 2D and 1D three-layer responses are different—this, too, is because of the $\hat{j}_{I=0}$ dependency on the geometry.

Finally, all solutions converge to zero at very high concentrations ($\Sigma_s \ll c_{\text{left}}$). This too, can be expected since at the limit $\Sigma_s \ll c_{\text{left}}$, the contribution of Σ_s in Eq. (13)

vanishes and all terms are nullified. In fact, for the case of 1L and nonsymmetric diffusion coefficients, $\hat{V}_{I=0}$ is given analytically by the Henderson equation [65,70,73]

$$\hat{V}_{I=0} = V_{\text{th}} \frac{D_+ - D_-}{D_+ + D_-} \ln C_r, \tag{30}$$

where D_+ and D_- are the diffusion coefficients of the positive and negative species. For symmetric diffusion coefficients, this voltage is zero.

3. Transport number, $\hat{\tau}$

The transport number, shown in Fig. 5(c), does not behave in a very surprising manner. First, when $\Sigma_s \gg \max(c_{\text{left}}, c_{\text{right}})$, the transport number is close to unity, such that the system is ideally selective. If $\Sigma_s \ll \min(c_{\text{left}}, c_{\text{right}})$, the transport number is close to one-half, such that the system is vanishingly selective. In between these two limits, when $\Sigma_s / c_{\text{left,right}} \sim 1$, the system is nonideally selective. Second, the transition region, i.e., the region in which the transport number changes from ½ to 1 (or vice versa), moves to higher concentrations as C_r is increased and is pushed to lower concentrations as C_r is decreased. Third, importantly, the transition region is always consonant with changes in other quantities, such as the change of $\hat{V}_{I=0}$ (at high concentrations and low concentrations) and the change in the Ohmic resistance discussed now.

4. The Ohmic resistance, R_{Ohmic}

The behavior of R_{Ohmic}, shown in Fig. 5(d), is complicated when accounting for the effects of the microchannels and when $C_r \neq 1$. To address this complexity, we shall start our analysis in the reverse order of complexity: (1) 1L and $C_r = 1$, (2) 1L and $C_r \neq 1$, (3) 3L and $C_r = 1$, and (4) 3L and $C_r \neq 1$.

1L and $C_r = 1$. At high concentrations ($\Sigma_s \ll c_{\text{left}}$), the resistance decreases with an inverse linear dependence on the bulk concentration (or the conductance scales linearly with concentration). This is a purely vanishingly selective system. At low concentrations ($\Sigma_s \gg c_{\text{left}}$), when the system is ideally selective, the resistance saturates to a value determined by Σ_s (this is the surface-charge-dominated regime). The transition from bulk-dominated to surface-charge dominated is correlated to the transport number transition shown in Fig. 5(c).

1L and $C_r \neq 1$. The response of the system does not qualitatively change much when $C_r \neq 1$. At high concentrations ($\Sigma_s \ll c_{\text{left}}$), the response is still determined by the bulk concentrations, where the higher of c_{left} and c_{right} plays a more important role here. At low concentrations, the response is still determined by Σ_s (which is still much larger than both c_{left} and c_{right}). The only change in the response between $C_r > 1$ and $C_r < 1$ is the concentration at which the resistance transitions from bulk-dominated to surface-dominated. This transition is correlated to the transport number transition shown in Fig. 5(c).

3L and $C_r = 1$. In contrast to the 1L scenario, the behavior of R_{Ohmic} for three layers with $C_r = 1$ (discussed thoroughly in Refs. [43,74]) is now divided into three regions: $\Sigma_s \ll c_{\text{left}}$, $\Sigma_s \sim c_{\text{left}}$ and $\Sigma_s \gg c_{\text{left}}$.

For $\Sigma_s \ll c_{\text{left}}$, R_{Ohmic} is still dominated by the bulk concentration. In 2D, R_{Ohmic} is dominated by $R_2 = L_2/H_2$, such that R_{Ohmic} overlaps with the 1L model and is virtually independent of the microchannel and field focusing resistances. However, in 1D, R_2 is no longer the dominant resistance and it is of the same order of magnitude as R_1 and R_3 such that the total resistance no longer overlaps with the 1L model.

Then, at $\Sigma_s \sim c_{\text{bulk}}$, for 2D, R_{Ohmic} is still dominated by the nanochannel, transitions from bulk (R_2) to surface charge dominated (R_2/Σ_s). Here, it appears that the total resistance is close to that of the 1L and $C_r = 1$ model. However, the similarities occur only for a small concentration range.

Then, for $\Sigma_s \gg c_{\text{bulk}}$, a second transition occurs. In contrast to $\Sigma_s \ll c_{\text{left}}$, when R_{Ohmic} is dominated by R_2, now the R_2/Σ_s term is subordinate to the $\Sigma R_1 + \Sigma R_3$ term (which is now the dominant term). However, the $\Sigma R_1 + \Sigma R_3$ term also scales inversely with the bulk concentration, leading to the additional increase of R_{Ohmic} with decreasing concentrations. The contributions of the microchannels and the field-focusing resistances are the reason the 3L-2D response and the 1L-1D response diverge at low concentrations [inset of Fig. 5(d)]. In 1D (wherein $H_{1,3} = H_2$), a similar transition that is virtually unobservable occurs. Here, the transition from $R_{\text{Ohmic}} \sim (L_1 + L_2 + L_3)$ to $R_{\text{Ohmic}} \sim (L_1 + L_3)$ occurs, but it occurs over a very small concentration range such that it is not truly observable.

3L and $C_r \neq 1$. Finally, the response of a three-layered 2D system for $C_r \neq 1$ [Eq. (18)] shares attributes with the 3L and $C_r = 1$ scenario, and the 1L and $C_r \neq 1$ scenario [Fig. 5(d)]. For $\Sigma_s \ll c_{\text{bulk}}$, R_{Ohmic} scales inversely with the bulk concentration but also depends on the higher of c_{left} and c_{right}. For $\Sigma_s \sim c_{\text{bulk}}$, the R_{Ohmic} is still dominated by R_2/Σ_s, where the concentration at which R_{Ohmic} transitions from R_2 to R_2/Σ_s depends on the value of C_r. At $\Sigma_s \gg c_{\text{bulk}}$, R_{Ohmic} is once more dominated by $\Sigma R_1(c_{\text{left}}) + \Sigma R_3(c_{\text{right}})$, which leads to the additional increase of R_{Ohmic} with decreasing concentrations, as well as the shift of the curve relative to the $C_r = 1$ curve. The additional resistances of $\Sigma R_1 + \Sigma R_3$ also have implications for the harvestable electrical current and electrical power discussed in the section below.

In principle, determining the dominant resistor is trivial once the geometry and the material have been specified. First, calculate the R functions given in Eq. (8). Then, determine Σ_s. We recommend that one use the $C_r = 1$ scenario, whose final expression for the resistance is

easier/simpler than that of the $C_r \neq 1$ scenario. Then, one can consider the various ratios of all the contributions. See Supplemental Material [35] for an additional discussion on this issue.

The analysis in Fig. 5 is for the case that $C_r = c_{\text{right}}/c_{\text{left}}$ is kept constant. One can also consider the case that for a given c_{left}, one varies c_{right} such that C_r is varied. Both approaches can be found in the literature. For the sake of completeness, we provide the complementary figure to Fig. 5 in Supplemental Material [35].

5. Power

For the sake of brevity, we have left the discussion of the power at $I = 0$ to the next section, where it will be compared to the power at $V = 0$.

V. ZERO VOLTAGE RESPONSE, $V = 0$

A. Harvestable electrical current and power

While the $I = 0$ crossover point is a key parameter for the initial characterization of nanofluidic (and biological) systems, the $V = 0$ is by far more important for energy harvesting purposes, as both the electrical current, $I_{V=0}$, and the harvestable power, $P_{V=0}$, are defined at this point. However, there are several misconceptions about calculating $P_{V=0}$ in a self-consistent manner. These misconceptions lead to incorrect estimations of the available power and efficiency, such that experimental results and theoretical predictions always differ—perhaps even by more than an order of magnitude!

For a simple Ohmic resistor, the power is given by Watt's law

$$P = IV. \tag{31}$$

Based on this definition, the power at the intercept points, $V = 0$ and $I = 0$, is zero, $P = 0$. To bypass this difficulty, it has been suggested that the power be calculated by

$$P_{\text{incorrect}} = I_{V=0}V_{I=0}. \tag{32}$$

While intuitive, this *expression is incorrect*, as it mixes the electrical current and voltage from two different states. In fact, often, one can find a different (and equally incorrect) variation whereby $P = I_{V=0}^2 R_{I=0}$, which is derived by inserting Ohm's law for a constant resistance ($V_{I=0} = I_{V=0}R$) into Eq. (32). The reason that Eq. (32) fails is because the resistance is not a constant (like in a metal), but rather it depends on the applied voltage (or resultant current), which creates a nonzero flux ($\hat{J}_{I=0}$). The simplest way to prove that this fails is to prove that the resistance is voltage (or current) dependent, such that $R_{V=0} \neq R_{I=0} = R_{\text{Ohmic}}$. We recently demonstrated this for a nanochannel-only system [65,70], where the resistance of a nanofluidic system, subject to a concentration gradient, varies with the voltage. In this work, we extend this observation and demonstrate that $R_{V=0} \neq R_{I=0}$ for a three-layered system as well. Below, we will show this graphically, and in Supplemental Material [35], we prove this mathematically.

Thus, before proceeding with the analysis, it is essential to establish the correct way to calculate the power. At the intercept points ($I = 0$ and $V = 0$), the power is given by

$$P_{I=0} = V_{I=0}^2/R_{\text{I=0}}, \tag{33}$$

and

$$P_{V=0} = I_{V=0}^2 R_{V=0}. \tag{34}$$

Equations (33) and (34) are internally consistent in that they do not mix quantities from two different states. They represent different power estimates. Equation (33) is the power at $I = 0$ (i.e., $P_{I=0}$), which can be calculated immediately since both $V_{I=0}$ and R_{Ohmic} are analytically known. However, this power is not related to the harvestable osmotic power. Rather, it is the power required to ensure that there are no flowing electrical currents in the system (i.e., equilibrium state). Equation (34) represents the harvestable osmotic power at $V = 0$.

To calculate $P_{V=0}$, two challenges need to be overcome: (1) How to calculate $I_{V=0}$? and (2) How to calculate $R_{V=0}$? The answer to both these questions lies, once more, within the two master equations [Eqs. (10) and (11)]. However, in contrast to our approach in Sec. IV A, wherein we resolved the expressions analytically, the approach here requires solving the master equations numerically. The details of the numerical methods are given in Supplemental Material [35].

Briefly, for a given set Σ_s, c_{left}, and c_{right}, we solve the $i - j$ relation [Eq. (11)] for a wide range of j to calculate i. We then insert the (i, j) pair into the $V(i, j)$ relation [Eq. (10)], which is subsequently scanned to find the nearest point to $V = 0$. We then perform a linear interpolation in the vicinity of this point to find the crossover point, which yields $I_{V=0}$. At this point, we also calculate the local slope

$$R_{V=0} = \left(\frac{dV}{dI}\right)_{V=0}, \tag{35}$$

which provides the value of the differential resistance required for calculating $P_{V=0}$ [Eq. (34)]. As we will show, the ratio $R_{V=0}/R_{I=0}$ can predict a factor of 2 change in the resistance, potentially leading to a 100% error.

The second, and perhaps more important, misconception is that the additional microchannel resistances are often neglected, with only the nanochannel resistance being accounted for. We will show that for the harvestable current and harvestable power, the 1L system has the

highest outputs. Upon inclusion of the microchannels (3L), the current and power show a substantial drop by orders of magnitude. This drop is obviously associated with the additional resistances of the microchannels, which are often ignored when interpreting experimental data. As a result, experimentalists are never able to attain the maximal predicted power, and, therefore, find various figures of merit to rationalize how one system is preferable over other systems. In reality, as we show in this work, once the geometry has been set (2D/3D versus 1D and 3L versus 1L) and the concentration gradient has been set (c_{left} and c_{right}), for a given Σ_s, the response is unequivocally determined, and figures of merit are not needed. The reader should also bear in mind that the 1L system is perhaps the best system, but engineering-wise, this system can never be attained experimentally since reservoirs are needed. Thus, one needs to use 3L systems where the effects of ΣR_k are reduced.

B. Results

We now present the complementary $V = 0$ analysis to the previous $I = 0$ analysis, but focus on different transport characteristics relevant to energy harvesting. For simplicity, we start our analysis with $R_{V=0}$. Then we consider the behavior of $I_{V=0}$ and conclude with $P_{V=0}$.

1. Zero-voltage resistance, $R_{V=0}$

Overall, the qualitative behavior of $R_{V=0}$ [Fig. 6(a)] is the same as that of $R_{I=0} = R_{\text{Ohmic}}$ [Fig. 5(d)], and as such, we do not repeat the discussion/analysis here. While there are no qualitative changes, there are some quantitative changes. These are best observed by considering the ratio $R_{V=0}/R_{I=0}$ [Fig. 6(b)], where it can be observed that this ratio deviates from unity. These differences, which vary with the scenarios, are very nuanced and require a thorough discussion. Similar to Sec. IV C 4, we will start our discussion from the simplest and work our way to the complicated systems. Finally, since here we will compare the results to those shown in the $I = 0$ section (Sec. IV C), we keep the heights to be $H_2 = H_1/500$.

1L-1D. At the two extreme limits of ideal (low concentrations) and vanishing (high concentrations) selectivity, the ratio $R_{V=0}/R_{I=0}$ is indeed unity (as was recently shown in Refs. [42,65]). However, at intermediate selectivity, the ratio $R_{V=0}/R_{I=0}$ exceeds unity, proving that $R_{V=0} \neq R_{I=0}$. The mathematical proof that $R_{V=0} \neq R_{I=0}$ for 1L-1D is given in Ref. [65].

3L-1D. As previously described and demonstrated in Fig. 5(d), in 1D, the nanochannel resistance no longer dominates the response. Rather, at low concentrations, the microchannel and field focusing resistances dominate the response once more. Here, too, they dominate the response [Fig. 6(a)]. It can be observed that at high concentrations, $R_{V=0}/R_{I=0}$ is unity and at low concentrations, $R_{V=0}/R_{I=0}$ is smaller than unity [Fig. 6(b)]. This result is consistent with the theoretical proof provided in Supplemental Material [35]. Notably, the bumps shown in Fig. 6(b) in the 1L-1D case do not appear here.

3L-2D. The 3L-2D scenario behaves like a combination of 1L-1D and 3L-1D scenarios. Like both previous scenarios, at high concentrations, $R_{V=0}/R_{I=0}$ is unity. However, at intermediate concentrations, bumps similar to those observed in the 1L-1D system are observed. The appearance of these bumps here can be attributed to the fact that, similar to the behavior of 2D R_{Ohmic} response in Fig. 5(d), the total response is once more dominated by the nanochannel (which does not occur in the 3L-1D scenario). However, at lower concentrations, also similar to the 2D R_{Ohmic} response shown in Fig. 5(d), the response is dominated by the microchannels (and associated field-focusing resistances). For the considered cases of $C_r = 10^{-1}$ and $C_r = 10$, the ratio varies from about 0.45 to 1.2. However, different values of C_r can lead to even

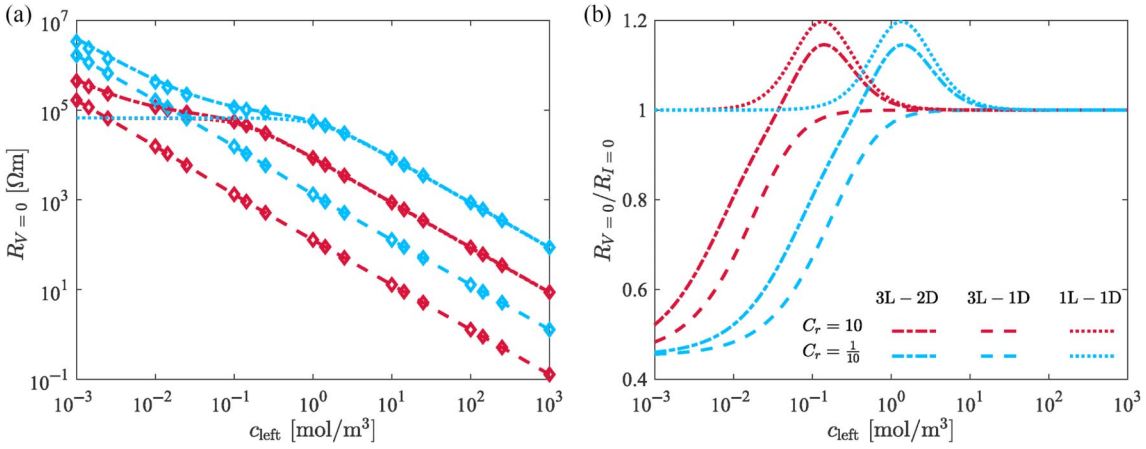

FIG. 6. (a) The zero-voltage resistance, $R_{V=0}$, and (b) the ratio $R_{V=0}/R_{I=0}$ versus the left concentration c_{left} for various geometries and different values of C_r (the details of the 2D geometry are given in Supplemental Material [35]). Markers represent COMSOL simulation data points.

larger deviations. Thus, suggesting using $R_{\mathrm{Ohmic}} = \hat{R}_{I=0}$ when $V = 0$ could yield errors of 10%–100% when estimating the resistance and the power.

Regardless, under no circumstances did we find a scenario in which $R_{V=0} \triangleq R_{I=0}$ for all concentrations or concentration ratios. This is why Eq. (32), which mixes quantities from two different states, is incorrect, and why one needs to use the self-consistent expressions given by Eqs. (33) and (34).

2. Zero-voltage current, $i_{V=0}$

Figures 7(a) and 7(b) display the zero-voltage current density, $i_{V=0}$, and the current, $I_{V=0}$, respectively, versus the left salt concentration. Three general observations are apparent. First, the response depends strongly on the geometry of the system (number of layers and the system's dimension, i.e., 1D or 2D). Second, independent of the geometry, $i_{V=0}$ changes signs as C_r crosses unity (similar to $\hat{j}_{I=0}$ and $\hat{V}_{I=0}$ in Fig. 5). Finally, we start the analysis with one layer and then move to three layers. Since the goal of RED is to maximize the harvestable energy current, it is preferable to consider systems with smaller resistances. Hence, here we will compare the harvestable current of the 1L system to the 3L-1D system by using $H_2 = H_1$.

1L-1D. For both $i_{V=0}$ and $I_{V=0}$, we find that this system has the largest currents (in the absolute sense). This should not be surprising since the 1L system has the smallest resistance among all considered scenarios. We further see that at the limits of ideal (low concentration) and vanishing selectivity (high concentration), the currents saturate to constant values. The transition between these two limits occurs more or less in the region where $\Sigma_s \sim O(c_{\mathrm{left}}, c_{\mathrm{right}})$, but not necessarily for the same concentration as for the resistance's transition [shown in Figs. 5(d) and 6], with a natural dependence on C_r. Importantly, at low concentrations, the saturated current value is not zero.

3L-1D and 3L-2D. The addition of the microchannels (whether in 1D or 2D) changes the response. The one apparent observation is that, for all concentrations, the current with microchannels is smaller than the current without microchannels. This is due to the addition of ΣR_k. That the addition of ΣR_k changes the response should no longer be surprising, as this has already been established in the analysis of Figs. 5(d) and 6.

For $I_{V=0}$, we have the expected result that the 3L-2D scenario, which accounts for both $R_{k=1,3}$ and $R_{\mathrm{FF},k=1,3}$, has the smallest current, while the 3L-1D scenario, which accounts only for $R_{k=1,3}$ has the intermediate current [Fig. 7(b)]. Importantly, as the concentration is decreased further, the increased resistance results in a continuously decreasing current, which will also lead to decreasing harvestable power density. In Fig. 7(a), we see a reversal of the behavior of $i_{V=0}$ for the 3L-1D and 3L-2D scenarios. The reversal of the behavior of the current density and current was previously reported in Refs. [44,45,75].

Perhaps the two most important outcomes of the analysis of Fig. 7 are that, for an "ideal" nanochannel-only (1L) system, the low-concentration harvestable current saturates to a finite and nonzero value. One can consider this value to be the upper limit of the available harvestable current. For the realistic system that accounts for microchannels (or larger reservoirs), the harvestable current converges to zero as concentrations decrease, resulting in a corresponding decrease in harvestable power. The other outcome is that the current of the 1L is substantially larger than with the microchannels (3L). We will demonstrate how these outcomes vary the behavior of the power. To that end, we will once more consider $H_2 = H_1$.

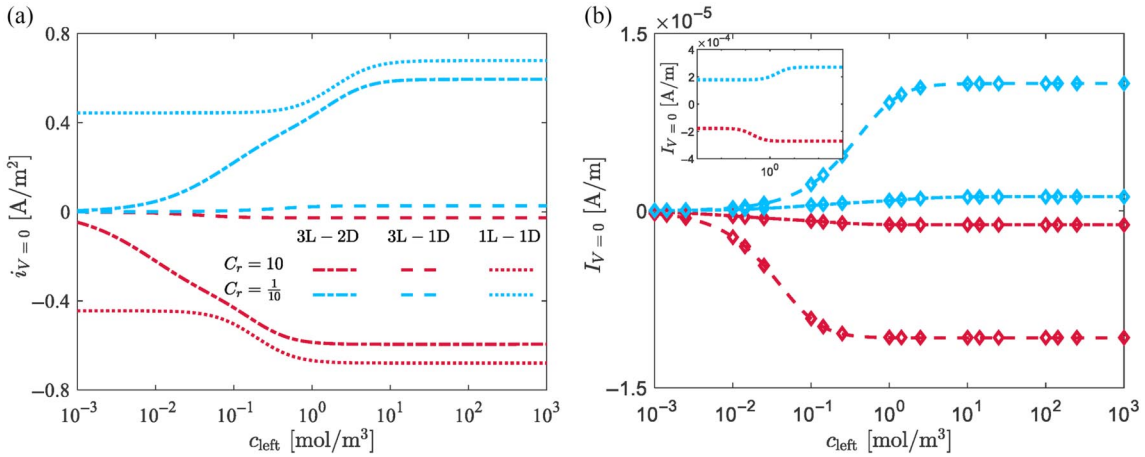

FIG. 7. (a) The zero-voltage current density, $i_{V=0}$, and (b) the current, $I_{V=0}$, versus the left concentration c_{left} for various geometries and different values of C_r (the details of the geometry are given in Supplemental Material [35]). To enhance the presentation of the $I_{V=0}$ plot on (b), the nanochannel-only (1L-1D) curves, which are substantially larger than the remaining curves, have been moved to the inset of (b). Markers represent COMSOL simulation data points.

3. Power

We start our analysis with the simpler zero-current power, $P_{I=0}$ [Eq. (33)]. Thereafter, we consider the zero-voltage power, $P_{V=0}$ [Eq. (34)] that can be harvested by RED systems. In both cases, we consider both the 2D power and the 1D power. Both of these can be considered to be power densities of the 3D power. For simplicity, we term the 2D power as the power and the 1D power as the power density.

Figures 8(a) and 8(b) show the expected result that the system with the largest harvestable power density and power, respectively, is the one-layered system, which is also the system with the smallest resistance. The behavior of the 1L system is easy to rationalize if one remembers that $P_{I=0}$ is a multiplication of the already known $\hat{V}_{I=0}$ [Eq. (13)] and $R_{\mathrm{Ohmic}} = \hat{R}_{I=0}$ [Eq. (18)]. At low concentrations, when $\hat{V}_{I=0}$ [Fig. 5(b)] and $R_{\mathrm{Ohmic}} = \hat{R}_{I=0}$ [Fig. 5(d)] saturate to a constant value, so does the power (or power density). At high concentrations, both $\hat{V}_{I=0}$ and $\hat{R}_{\mathrm{Ohmic}}$ converge to zero. Thus, the power decreases accordingly.

The addition of the diffusion layers/microchannels (3L) changes the response in an expected manner. At low concentrations, $\hat{V}_{I=0}$ is still given by a constant, but $\hat{R}_{\mathrm{Ohmic}}$ increases with decreasing concentrations, such that the power [Fig. 8(b)] must decrease as well. Thus, it can be expected that there exists a concentration for which the power is maximal. As we will show shortly, there is an optimal power also for $V = 0$. For energy harvesting purposes, one would like to operate as closely as possible to this point. For physiological purposes ($I = 0$), arguments can be made about why certain processes occur far away from this point, but also why other processes take place at this point.

Naturally, the 1D system whose microchannel resistances ($\Sigma R_1 + \Sigma R_3$) are smaller than those of the 2D system has a larger power. However, in Fig. 8(a), it can be observed that the power density of the 3L-2D system is larger than that of the 3L-1D system. Such a behavior has been reported in past works [44,45,75]. This is because the current is squeezed into a smaller cross section. At high concentrations, the power decreases for the same reason that the 1L system decreases (i.e., the decrease of $\hat{V}_{I=0}$ and R_{Ohmic}).

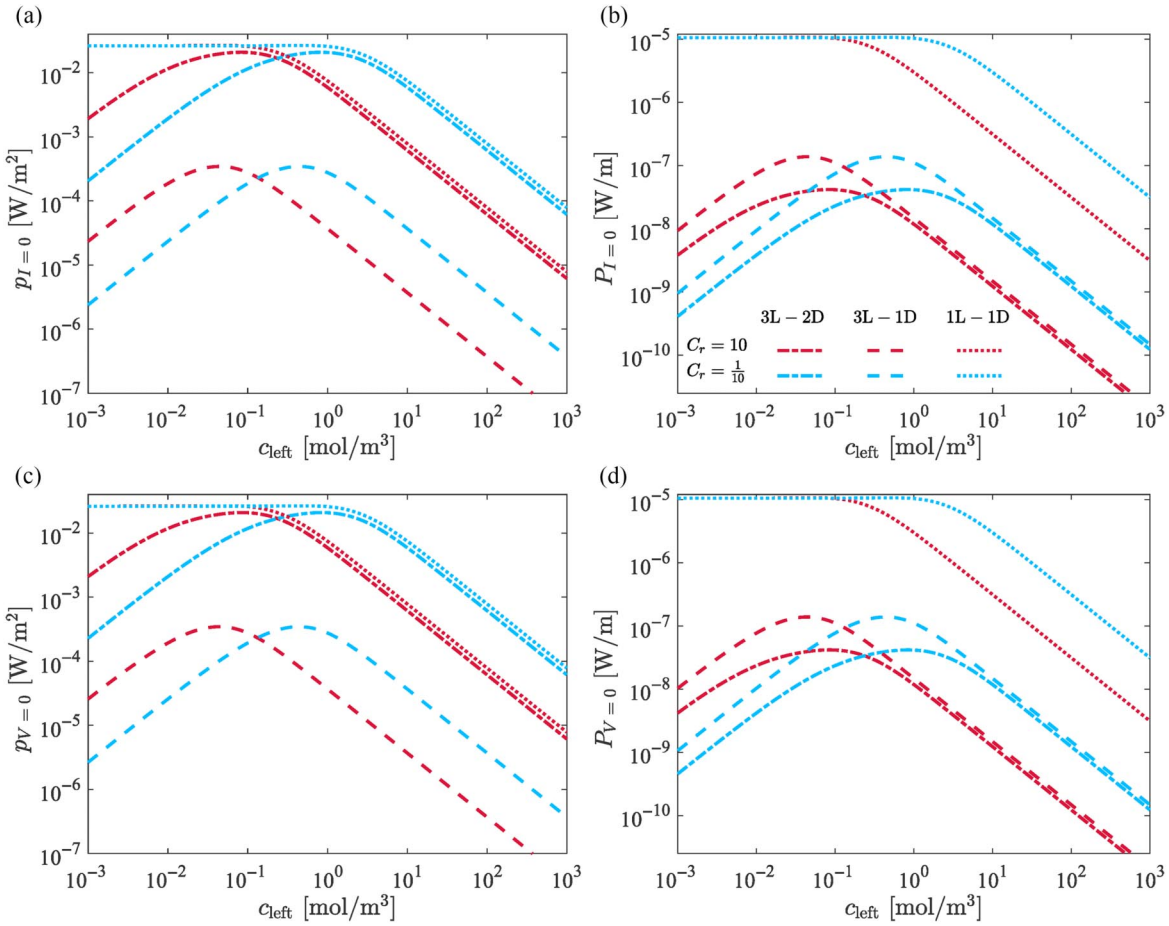

FIG. 8. Zero-current (top row) and zero-voltage (bottom row) power density p (a),(c) and power P (b),(d) versus the left concentration c_{left} for various geometries and different values of C_r (the details of the geometry are given in Supplemental Material [35]).

As we transition to $V = 0$, we should remember two things. First, while $R_{V=0}$ [Fig. 6(a)] behaves qualitatively in a very similar manner to $\hat{R}_{I=0}$ [Fig. 5(d)], there are some quantitative changes [Fig. 6(b)]. Second, similar to $\hat{V}_{I=0}$, which has a sigmoidlike behavior (in the logarithmic sense on the concentration axis), $I_{V=0}$ also has a sigmoidlike behavior [Fig. 7(b)]. At low concentrations, the curve is a finite constant, while at high concentrations, it converges to zero. Thus, in a very unsurprising manner, the curves of the power density and power of $P_{V=0}$ are very similar to those of $P_{I=0}$—to the eye, one might even consider them to be identical—we will shortly show that they are not. However, beforehand, it is essential to point out the key finding of Fig. 8(b) [and perhaps Fig. 8(d)]: the power of a realistic 3L system is several orders of magnitude smaller than the idealized 1L system. In order for realistic RED systems to achieve their "ideal" potential, one needs to reduce the resistance of the microchannels. This can be done by placing the electrodes as closely as possible to the 1D membranes.

The ratio $P_{V=0}/P_{I=0}$ is shown in Fig. 9. For the 1L system, the ratio is near unity for all concentrations. However, a "double-bump"-like feature can be observed. This feature can be rationalized thus. One of these bumps is attributed to the bump $R_{V=0}/R_{I=0}$ shown in Fig. 6, while the other bump can be attributed to the fact that the transition concentration of each of the respective sigmoid curves of $\hat{V}_{I=0}$ and $I_{V=0}$ is different [Figs. 5(b) and 7, respectively]. For the 3L systems, the double-bump is observed for the same reasons, but we also see that at low concentrations $P_{V=0} < P_{I=0}$. This is because $R_{V=0} < R_{I=0}$ (Fig. 6).

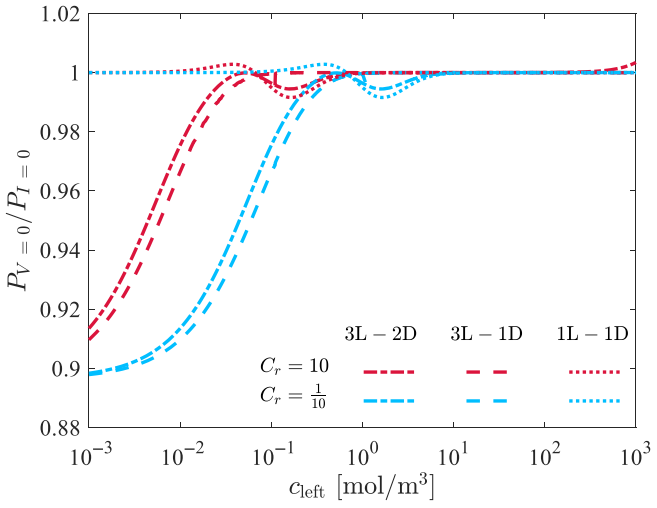

FIG. 9. The ratio $P_{V=0}/P_{I=0}$ versus the left concentration c_{left} for various geometries and different values of C_r (the details of the 2D geometry are given in Supplemental Material [35]).

VI. CONCLUSIONS

In this work, we have addressed an identified knowledge gap—how to self-consistently characterize the response of a nanofluidic system comprised of a nanochannel and two adjoining microchannels, when subjected to an arbitrary concentration gradient. To that end, we have derived two self-consistent master equations [Eqs. (10) and (11)] for the current density-voltage response ($i - V$) and the salt flux-electrical current density relation ($i - j$). These two master equations are then analyzed in the two important operational limits: zero-current ($I = 0$) and zero-voltage ($V = 0$). As such, we divide this Conclusion section accordingly.

For the limiting case of $I = 0$ (Sec. IV), we are able to approximate these two equations and derive analytical expressions for all transport characteristics (salt current at zero-electrical current, $\hat{J}_{I=0}$, zero-electrical current voltage, $\hat{V}_{I=0}$, the equilibrium transport number, $\hat{\tau}$, and the Ohmic resistance, $R_{\text{Ohmic}} = \hat{R}_{I=0}$). Not only can the newly derived model be reduced to three previously derived models (Supplemental Material [35]), but it also has new predictive capabilities, which, for brevity, are not repeated here in detail. In short, we have shown that the 3L and $C_r \neq 1$ model exhibits characteristics of both the 3L and $C_r = 1$ model and the 1L and $C_r \neq 1$ model (Fig. 5).

For the limiting case of $V = 0$ (Sec. V), analytical solutions for the master equations are no longer feasible, and numerical evaluation is required to calculate the transport characteristics. In particular, we show that $R_{V=0}/R_{I=0} \neq 1$ [Fig. 6(b)], which alone can lead to a substantial error in the comparison of experiments with theory. Importantly, in this section, we showed that the additional contribution of the microchannels (3L) varies the response relative to the 1L system in very nontrivial manners. In particular, the added contribution of the microchannels reduces the harvestable current, $I_{V=0}$, and harvestable power, $P_{V=0}$, in a substantial and non-negligible manner—by several orders of magnitude (where the exact value depends on the microchannel geometry, Figs. 7 and 8). Once the microchannels are accounted for, both the harvestable current and power have optimums that are close but do not exactly coincide. This emphasizes the importance of reducing the microchannel resistances as much as possible and realizing that the 3L-1D (nanoporous membrane) scenario has the optimal geometry, at least relative to the 3L-2D nanochannel geometry.

This work should be regarded as a foundational contribution to the theoretical description of ion transport characteristics in realistic nanofluidic systems, as our model (and analysis of its results) provides, to the best

of our knowledge, the most self-consistent and comprehensive framework to date for improving the performance of desalination and energy harvesting, as well as increasing our understanding of simple physiological systems.

ACKNOWLEDGMENTS

This work was supported by Israel Science Foundation Grant No. 204/25. We acknowledge the support of the Ilse Katz Institute for Nanoscale Science & Technology and the Pearlstone Center for Aeronautical Engineering Studies. R. A.-R. further acknowledges the support of Israel Science Foundation Grant No. 547/23. We thank Tomer Miara for his assistance with some of the illustration.

DATA AVAILABILITY

The data that support the findings of this article are not publicly available. The data are available from the authors upon reasonable request.

[1] A. Alcaraz, M. L. López, M. Queralt-Martín, and V. M. Aguilella, *Ion transport in confined geometries below the nanoscale: Access resistance dominates protein channel conductance in diluted solutions*, ACS Nano **11**, 10392 (2017).

[2] L. M. Alvero-González, M. Aguilella-Arzo, D. Aurora Perini, L. A. Bergdoll, M. Queralt-Martín, and A. Alcaraz, *Supralinear scaling behavior of ionic transport in membrane nanochannels regulated by outer-surface charges*, Nanoscale Adv. **6**, 6344 (2024).

[3] E. Cao and Z. S. Siwy, *Leaving constraints of single nanopores and designing biomimetic nanopore arrays*, Curr. Opin. Electrochem. **51**, 101677 (2025).

[4] S. J. Kim, S. H. Ko, K. H. Kang, and J. Han, *Direct seawater desalination by ion concentration polarization*, Nat. Nanotechnol. **5**, 297 (2010).

[5] L. Bocquet and E. Charlaix, *Nanofluidics, from bulk to interfaces*, Chem. Soc. Rev. **39**, 1073 (2010).

[6] N. Kavokine, R. R. Netz, and L. Bocquet, *Fluids at the nanoscale: From continuum to subcontinuum transport*, Annu. Rev. Fluid Mech. **53**, 377 (2021).

[7] A. Keerthi, S. Goutham, Y. You, P. Iamprasertkun, R. A. W. Dryfe, A. K. Geim, and B. Radha, *Water friction in nanofluidic channels made from two-dimensional crystals*, Nat. Commun. **12**, 3092 (2021).

[8] F. H. J. van der Heyden, D. Stein, and C. Dekker, *Streaming currents in a single nanofluidic channel*, Phys. Rev. Lett. **95**, 116104 (2005).

[9] A. Siria, P. Poncharal, A.-L. Biance, R. Fulcrand, X. Blase, S. T. Purcell, and L. Bocquet, *Giant osmotic energy conversion measured in a single transmembrane boron nitride nanotube*, Nature (London) **494**, 455 (2013).

[10] J. Feng, M. Graf, K. Liu, D. Ovchinnikov, D. Dumcenco, M. Heiranian, V. Nandigana, N. R. Aluru, A. Kis, and A. Radenovic, *Single-layer* MoS_2 *nanopores as nanopower generators*, Nature (London) **536**, 197 (2016).

[11] A. Siria, M.-L. Bocquet, and L. Bocquet, *New avenues for the large-scale harvesting of blue energy*, Nat. Rev. Chem. **1**, 0091 (2017).

[12] Q. Wang, X. Zhang, H. Zhu, X. Zhang, Q. Liu, M. Fu, J. Zhu, J. Pu, and Z. Qu, *Nanochannel-based ion transport and its application in osmotic energy conversion: A critical review*, Adv. Phys. Res. **2**, 2300016 (2023).

[13] S. Chakraborty, C. Bakli, D. Roy, A. Chaudhuri, A. Guha, and A. Patwari, *Electrokinetic energy harvesting over nanometer and sub-nanometer scales*, Appl. Phys. Rev. **12**, 011305 (2025).

[14] H. Strathmann, *Ion-Exchange Membrane Separation Processes* (Elsevier, New York, 2004).

[15] A. Meller, L. Nivon, and D. Branton, *Voltage-driven DNA translocations through a nanopore*, Phys. Rev. Lett. **86**, 3435 (2001).

[16] I. Vlassiouk, T. R. Kozel, and Z. S. Siwy, *Biosensing with nanofluidic diodes*, J. Am. Chem. Soc. **131**, 8211 (2009).

[17] B. Nadler, Z. Schuss, U. Hollerbach, and R. S. Eisenberg, *Saturation of conductance in single ion channels: The blocking effect of the near reaction field*, Phys. Rev. E **70**, 051912 (2004).

[18] A. Meller, *A new tool for cell signalling research*, Nat. Nanotechnol. **14**, 732 (2019).

[19] M. Aramesh *et al.*, *Localized detection of ions and biomolecules with a force-controlled scanning nanopore microscope*, Nat. Nanotechnol. **14**, 791 (2019).

[20] M. Wanunu, W. Morrison, Y. Rabin, A. Y. Grosberg, and A. Meller, *Electrostatic focusing of unlabelled DNA into nanoscale pores using a salt gradient*, Nat. Nanotechnol. **5**, 160 (2010).

[21] M. Wanunu, T. Dadosh, V. Ray, J. Jin, L. McReynolds, and M. Drndić, *Rapid electronic detection of probe-specific microRNAs using thin nanopore sensors*, Nat. Nanotechnol. **5**, 807 (2010).

[22] M. Wanunu, J. Sutin, and A. Meller, *DNA profiling using solid-state nanopores: Detection of DNA-binding molecules*, Nano Lett. **9**, 3498 (2009).

[23] D. Branton *et al.*, *The potential and challenges of nanopore sequencing*, Nat. Biotech. **26**, 1146 (2008).

[24] J. G. Hedley, K. Coshic, A. Aksimentiev, and A. A. Kornyshev, *Electric field of DNA in solution: Who Is in charge?*, Phys. Rev. X **14**, 031042 (2024).

[25] A. Aksimentiev, *Thread, read, rewind, repeat: Towards using nanopores for protein sequencing*, Nature (London) **633**, 533 (2024).

[26] T. Emmerich, N. Ronceray, K. V. Agrawal, S. Garaj, M. Kumar, A. Noy, and A. Radenovic, *Nanofluidics*, Nat. Rev. Methods Primer **4**, 69 (2024).

[27] N. Soni, Z. Rosenstock, N. C. Verma, K. Siddharth, N. Talor, J. Liu, B. Marom, A. B. Kolomeisky, A. Aksimentiev, and A. Meller, *Full-length protein classification via cysteine fingerprinting in solid-state nanopores*, Nat. Nanotechnol. **20**, 1482 (2025).

[28] R. E. Pattle, *Production of electric power by mixing fresh and salt water in the hydroelectric pile*, Nature (London) **174**, 660 (1954).

[29] G. W. Murphy, H. H. Steinhauser, and R. C. Taber, *The Minimum Energy Requirements for Sea Water Conversion Processes* (U.S. Dept. of the Interior, Washington, D.C, 1956).

[30] O. Levenspiel and N. de Nevers, *The osmotic pump*, Science **183**, 157 (1974).

[31] G. Belfort and G. A. Guter, *An electrical analogue for electrodialysis*, Desalination **5**, 267 (1968).

[32] J. N. Weinstein and F. B. Leitz, *Electric power from differences in salinity: The dialytic battery*, Science **191**, 557 (1976).

[33] R. E. Lacey, *Energy by reverse electrodialysis*, Ocean Eng. **7**, 1 (1980).

[34] N. Y. Yip, D. A. Vermaas, K. Nijmeijer, and M. Elimelech, *Thermodynamic, energy efficiency, and power density analysis of reverse electrodialysis power generation with natural salinity gradients*, Environ. Sci. Technol. **48**, 4925 (2014).

[35] See Supplemental Material at http://link.aps.org/supplemental/10.1103/xnd6-226l for a table of nomenclature, additional information on the derivation of the solution, additional discussions, and supplemental figures, which also includes Refs. [76–112], (n.d.).

[36] C. Zhu, P. Liu, B. Niu, Y. Liu, W. Xin, W. Chen, X.-Y. Kong, Z. Zhang, L. Jiang, and L. Wen, *Metallic two-dimensional* MoS_2 *composites as high-performance osmotic energy conversion membranes*, J. Am. Chem. Soc. **143**, 2021 (1932).

[37] Y.-C. Yao, A. Taqieddin, M. A. Alibakhshi, M. Wanunu, N. R. Aluru, and A. Noy, *Strong electroosmotic coupling dominates ion conductance of 1.5 nm diameter carbon nanotube porins*, ACS Nano **13**, 12851 (2019).

[38] B. Hille, *Ion Channels of Excitable Membranes*, 3rd ed. (Sinauer Associate, Sunderland, Mass, 2001).

[39] J. Melcr, D. Bonhenry, Š. Timr, and P. Jungwirth, *Transmembrane potential modeling: Comparison between methods of constant electric field and ion Imbalance*, J. Chem. Theory Comput. **12**, 2418 (2016).

[40] X. Lin and A. A. Gorfe, *Transmembrane potential of physiologically relevant model membranes: Effects of membrane asymmetry*, J. Chem. Phys. **153**, 105103 (2020).

[41] Z. Li, R. P. Misra, Y. Li, Y.-C. Yao, S. Zhao, Y. Zhang, Y. Chen, D. Blankschtein, and A. Noy, *Breakdown of the Nernst–Einstein relation in carbon nanotube porins*, Nat. Nanotechnol. **18**, 2 (2023).

[42] O. Lavi and Y. Green, *A theoretical characterization of osmotic power generation in nanofluidic systems*, Commun. Mater. **5**, 1 (2024).

[43] Y. Green, R. Abu-Rjal, and R. Eshel, *Electrical resistance of nanochannel-microchannel systems: an exact solution*, Phys. Rev. Appl. **14**, 014075 (2020).

[44] Y. Green, S. Shloush, and G. Yossifon, *Effect of geometry on concentration polarization in realistic heterogeneous permselective systems*, Phys. Rev. E **89**, 043015 (2014).

[45] J. Sebastian and Y. Green, *Electrical circuit modeling of nanofluidic systems*, Adv. Phys. Res. **2**, 2300044 (2023).

[46] Z. Siwy, E. Heins, C. C. Harrell, P. Kohli, and C. R. Martin, *Conical-nanotube ion-current rectifiers: The role of surface charge*, J. Am. Chem. Soc. **126**, 10850 (2004).

[47] I. Vlassiouk, S. Smirnov, and Z. Siwy, *Nanofluidic ionic diodes. Comparison of analytical and numerical solutions*, ACS Nano **2**, 1589 (2008).

[48] Y. He, D. Gillespie, D. Boda, I. Vlassiouk, R. S. Eisenberg, and Z. S. Siwy, *Tuning transport properties of nanofluidic devices with local charge inversion*, J. Am. Chem. Soc. **131**, 5194 (2009).

[49] C. B. Picallo, S. Gravelle, L. Joly, E. Charlaix, and L. Bocquet, *Nanofluidic osmotic diodes: Theory and molecular dynamics simulations*, Phys. Rev. Lett. **111**, 244501 (2013).

[50] Z. Ható, M. Valiskó, T. Kristóf, D. Gillespie, and D. Boda, *Multiscale modeling of a rectifying bipolar nanopore: Explicit-water versus implicit-water simulations*, Phys. Chem. Chem. Phys. **19**, 17816 (2017).

[51] E. Mádai, M. Valiskó, and D. Boda, *Application of a bipolar nanopore as a sensor: Rectification as an additional device function*, Phys. Chem. Chem. Phys. **21**, 19772 (2019).

[52] R. A. Lucas and Z. S. Siwy, *Tunable nanopore arrays as the basis for ionic circuits*, ACS Appl. Mater. Interfaces **12**, 56622 (2020).

[53] A. Córdoba, J. M. M. de Oca, J. Dhanasekaran, S. B. Darling, and J. J. de Pablo, *Current rectification by nanoparticles in bipolar nanopores*, Mol. Syst. Des. Eng. **8**, 289 (2023).

[54] A. Ben-Kish Sharvit and Y. Green, *Towards a unified mechanistic understanding of the electrical response of bipolar membrane systems*, J. Membr. Sci. **754**, 125628 (2026).

[55] E. Mádai, B. Matejczyk, A. Dallos, M. Valiskó, and D. Boda, *Controlling ion transport through nanopores: Modeling transistor behavior*, Phys. Chem. Chem. Phys. **20**, 24156 (2018).

[56] A. Noy, Z. Li, and S. B. Darling, *Fluid learning: Mimicking brain computing with neuromorphic nanofluidic devices*, Nano Today **53**, 102043 (2023).

[57] T. Teorell, *An attempt to formulate a quantitative theory of membrane permeability*, Proc. Soc. Exp. Biol. Med. **33**, 282 (1935).

[58] K. H. Meyer and J.-F. Sievers, *La perméabilité des membranes I. Théorie de la perméabilité ionique*, Helv. Chim. Acta **19**, 649 (1936).

[59] A. H. Galama, J. W. Post, H. V. M. Hamelers, V. V. Nikonenko, and P. M. Biesheuvel, *On the origin of the membrane potential arising across densely charged ion exchange membranes: How well does the Teorell-Meyer-Sievers theory work?*, J. Membr. Sci. Res. **2**, 128 (2016).

[60] J. Schaep and C. Vandecasteele, *Evaluating the charge of nanofiltration membranes*, J. Membr. Sci. **188**, 129 (2001).

[61] E. Secchi, A. Niguès, L. Jubin, A. Siria, and L. Bocquet, *Scaling behavior for ionic transport and its fluctuations in individual carbon nanotubes*, Phys. Rev. Lett. **116**, 154501 (2016).

[62] P. M. Biesheuvel and M. Z. Bazant, *Analysis of ionic conductance of carbon nanotubes*, Phys. Rev. E **94**, 050601 (2016).
[63] Y. Green, *Effects of surface-charge regulation, convection, and slip lengths on the electrical conductance of charged nanopores*, Phys. Rev. Fluids **7**, 013702 (2022).
[64] Y. Green, *Ion transport in nanopores with highly overlapping electric double layers*, J. Chem. Phys. **154**, 084705 (2021).
[65] Y. Green, *Goldman-Hodgkin-Katz equation, reverse electrodialysis, and everything in between*, Phys. Rev. E **111**, 064408 (2025).
[66] Y. Green, *Current-voltage response for unipolar funnel-shaped nanochannel diodes*, Phys. Rev. E **98**, 033114 (2018).
[67] R. Abu-Rjal, V. Chinaryan, M. Z. Bazant, I. Rubinstein, and B. Zaltzman, *Effect of concentration polarization on permselectivity*, Phys. Rev. E **89**, 012302 (2014).
[68] R. Abu-Rjal and Y. Green, *Bipolar nanochannels: A systematic approach to asymmetric problems*, ACS Appl. Mater. Interfaces **13**, 27622 (2021).
[69] J. E. Hall, *Access resistance of a small circular pore*, J. Gen. Physiol. **66**, 531 (1975).
[70] Y. Green, *Universal model for ion transport: Bridging the Goldman-Hodgkin-Katz paradigm with reverse electrodialysis*, Phys. Rev. Lett. **134**, 228401 (2025).
[71] P. B. Peters, R. van Roij, M. Z. Bazant, and P. M. Biesheuvel, *Analysis of electrolyte transport through charged nanopores*, Phys. Rev. E **93**, 053108 (2016).
[72] L. Bocquet, *Diffusio-osmotic transport in nanochannels*, arXiv:2605.02419.
[73] J. W. Perram and P. J. Stiles, *On the nature of liquid junction and membrane potentials*, Phys. Chem. Chem. Phys. **8**, 4200 (2006).
[74] R. Abu-Rjal, Z. S. Siwy, and Y. Green, *Electrical response of nanofluidic systems subjected to viscosity gradients*, Phys. Rev. E **111**, 2025
[75] Y. Green and G. Yossifon, *Effects of three-dimensional geometric field focusing on concentration polarization in a heterogeneous permselective system*, Phys. Rev. E **89**, 013024 (2014).
[76] Householder, *Numerical Treatment of a Single Nonlinear Equation* (McGraw Hill, New York, 1970).
[77] I. Rubinstein, *Electro-Diffusion of Ions* (SIAM, Philadelphia, PA, 1990).
[78] I. Rubinstein and L. Shtilman, *Voltage against current curves of cation exchange membranes*, J. Chem. Soc. Faraday Trans. **2**, 231 (1979).
[79] I. Rubinstein and B. Zaltzman, *Electro-osmotically induced convection at a permselective membrane*, Phys. Rev. E **62**, 2238 (2000).
[80] S. S. Dukhin, V. N. Shilov, and J. J. Bikerman, *Dielectric phenomena and double layer in disperse systems and polyelectrolytes*, J. Electrochem. Soc. **121**, 154C (1974).
[81] G. Yossifon, P. Mushenheim, Y.-C. Chang, and H.-C. Chang, *Nonlinear current-voltage characteristics of nanochannels*, Phys. Rev. E **79**, 046305 (2009).
[82] Y. Green, Y. Edri, and G. Yossifon, *Asymmetry-induced electric current rectification in permselective systems*, Phys. Rev. E **92**, 033018 (2015).
[83] Y. Green, R. Eshel, S. Park, and G. Yossifon, *Interplay between nanochannel and microchannel resistances*, Nano Lett. **16**, 2744 (2016).
[84] M. B. Andersen, M. van Soestbergen, A. Mani, H. Bruus, P. M. Biesheuvel, and M. Z. Bazant, *Current-induced membrane discharge*, Phys. Rev. Lett. **109**, 108301 (2012).
[85] C. P. Nielsen and H. Bruus, *Transport-limited water splitting at ion-selective interfaces during concentration polarization*, Phys. Rev. E **89**, 042405 (2014).
[86] E. V. Dydek, B. Zaltzman, I. Rubinstein, D. S. Deng, A. Mani, and M. Z. Bazant, *Overlimiting current in a microchannel*, Phys. Rev. Lett. **107**, 118301 (2011).
[87] S. M. Rubinstein, G. Manukyan, A. Staicu, I. Rubinstein, B. Zaltzman, R. G. H. Lammertink, F. Mugele, and M. Wessling, *Direct observation of a nonequilibrium electro-osmotic instability*, Phys. Rev. Lett. **101**, 236101 (2008).
[88] G. Yossifon and H.-C. Chang, *Selection of nonequilibrium overlimiting currents: Universal depletion layer formation dynamics and vortex instability*, Phys. Rev. Lett. **101**, 254501 (2008).
[89] S. J. Kim, Y.-C. Wang, J. H. Lee, H. Jang, and J. Han, *Concentration polarization and nonlinear electrokinetic flow near a nanofluidic channel*, Phys. Rev. Lett. **99**, 044501 (2007).
[90] B. Zaltzman and I. Rubinstein, *Electro-osmotic slip and electroconvective instability*, J. Fluid Mech. **579**, 173 (2007).
[91] I. Rubinstein and B. Zaltzman, *Equilibrium electroconvective instability*, Phys. Rev. Lett. **114**, 114502 (2015).
[92] V. S. Pham, Z. Li, K. M. Lim, J. K. White, and J. Han, *Direct numerical simulation of electroconvective instability and hysteretic current-voltage response of a permselective membrane*, Phys. Rev. E **86**, 2012
[93] C. L. Druzgalski, M. B. Andersen, and A. Mani, *Direct numerical simulation of electroconvective instability and hydrodynamic chaos near an ion-selective surface*, Phys. Fluids **25**, 110804 (2013).
[94] E. A. Demekhin, N. V. Nikitin, and V. S. Shelistov, *Direct numerical simulation of electrokinetic instability and transition to chaotic motion*, Phys. Fluids **25**, 122001 (2013).
[95] R. Abu-Rjal, N. Leibowitz, S. Park, B. Zaltzman, I. Rubinstein, and G. Yossifon, *Signature of electroconvective instability in transient galvanostatic and potentiostatic modes in a microchannel-nanoslot device*, Phys. Rev. Fluids **4**, 084203 (2019).
[96] G. S. Ganchenko, E. N. Kalaydin, J. Schiffbauer, and E. A. Demekhin, *Modes of electrokinetic instability for imperfect electric membranes*, Phys. Rev. E **94**, 063106 (2016).
[97] R. Abu-Rjal, I. Rubinstein, and B. Zaltzman, *Driving factors of electro-convective instability in concentration polarization*, Phys. Rev. Fluids **1**, 023601 (2016).
[98] R. Abu-Rjal, L. Prigozhin, I. Rubinstein, and B. Zaltzman, *Equilibrium electro-convective instability in concentration polarization: The effect of non-equal ionic diffusivities and longitudinal flow*, Russ. J. Electrochem. **53**, 903 (2017).
[99] E. A. Demekhin, G. S. Ganchenko, and E. N. Kalaydin, *Transition to electrokinetic instability near imperfect charge-selective membranes*, Phys. Fluids **30**, 082006 (2018).

[100] R. Abu-Rjal and Y. Green, *Bipolar nanochannels: The effects of an electroosmotic instability. Part 1. Steady-state response*, Flow **4**, E28 (2024).

[101] R. Abu-Rjal and Y. Green, *Bipolar nanochannels: The effects of an electroosmotic instability. Part 2. Time-transient response*, Flow **4**, E29 (2024).

[102] O. Schnitzer and E. Yariv, *Electric conductance of highly selective nanochannels*, Phys. Rev. E **87**, 054301 (2013).

[103] R. H. Tunuguntla, R. Y. Henley, Y.-C. Yao, T. A. Pham, M. Wanunu, and A. Noy, *Enhanced water permeability and tunable ion selectivity in subnanometer carbon nanotube porins*, Science **357**, 792 (2017).

[104] J. K. Holt, H. G. Park, Y. Wang, M. Stadermann, A. B. Artyukhin, C. P. Grigoropoulos, A. Noy, and O. Bakajin, *Fast mass transport through sub-2-nanometer carbon nanotubes*, Science **312**, 1034 (2006).

[105] Y. Uematsu, R. R. Netz, L. Bocquet, and D. J. Bonthuis, *Crossover of the power-law exponent for carbon nanotube conductivity as a function of salinity*, J. Phys. Chem. B **122**, 2992 (2018).

[106] S. Balme, F. Picaud, M. Manghi, J. Palmeri, M. Bechelany, S. Cabello-Aguilar, A. Abou-Chaaya, P. Miele, E. Balanzat, and J. M. Janot, *Ionic transport through sub-10 nm diameter hydrophobic high-aspect ratio nanopores: Experiment, theory and simulation*, Sci. Rep. **5**, 10135 (2015).

[107] Y. Noh and N. R. Aluru, *Ion transport in electrically imperfect nanopores*, ACS Nano **14**, 10518 (2020).

[108] D. Stein, M. Kruithof, and C. Dekker, *Surface-charge-governed ion transport in nanofluidic channels*, Phys. Rev. Lett. **93**, 035901 (2004).

[109] E. Secchi, S. Marbach, A. Niguès, D. Stein, A. Siria, and L. Bocquet, *Massive radius-dependent flow slippage in carbon nanotubes*, Nature (London) **537**, 210 (2016).

[110] M. Manghi, J. Palmeri, K. Yazda, F. Henn, and V. Jourdain, *Role of charge regulation and flow slip in the ionic conductance of nanopores: An analytical approach*, Phys. Rev. E **98**, 012605 (2018).

[111] J. Schiffbauer and G. Yossifon, *Role of electro-osmosis in the impedance response of microchannel-nanochannel interfaces*, Phys. Rev. E **86**, 056309 (2012).

[112] E. Yariv, *Asymptotic current-voltage relations for currents exceeding the diffusion limit*, Phys. Rev. E **80**, 051201 (2009).